REPORT DOCUMENTATION PAGE	Form Approved OMB No. 0704-0188

1a REPORT SECURITY CLASSIFICATION Unclassified	1b RESTRICTIVE MARKINGS

2a SECURITY CLASSIFICATION AUTHORITY	3 DISTRIBUTION/AVAILABILITY OF REPORT Approved for public release; distribution unlimited
2b DECLASSIFICATION/DOWNGRADING SCHEDULE	

4 PERFORMING ORGANIZATION REPORT NUMBER(S)	5 MONITORING ORGANIZATION REPORT NUMBER(S)

6a NAME OF PERFORMING ORGANIZATION Research Service (151) Tucson VA Medical Center	6b OFFICE SYMBOL (If applicable)	7a NAME OF MONITORING ORGANIZATION

6c ADDRESS (City, State, and ZIP Code) Tucson, Arizona 85723	7b ADDRESS (City, State, and ZIP Code)

8a NAME OF FUNDING/SPONSORING ORGANIZATION U.S. Army Medical Research & Development Command	8b OFFICE SYMBOL (If applicable)	9 PROCUREMENT INSTRUMENT IDENTIFICATION NUMBER Army Project Order No. 87PP7853

8c ADDRESS (City, State, and ZIP Code) Fort Detrick Frederick, Maryland 21701-5012			

10 SOURCE OF FUNDING NUMBERS

PROGRAM ELEMENT NO.	PROJECT NO. 3M1	TASK NO.	WORK UNIT ACCESSION NO.
627770A	62770A871	AB	361

11. TITLE (Include Security Classification) Microvascular Physiologic and Anatomic Responses of the Guinea Pig to Experimental Arenavirus Infection

12. PERSONAL AUTHOR(S) Katz, Murray Allan

13a. TYPE OF REPORT Midterm	13b. TIME COVERED FROM 7/1/87 TO 2/28/89	14. DATE OF REPORT (Year, Month, Day) 1989 March 25	15. PAGE COUNT 64

16. SUPPLEMENTARY NOTATION

17. COSATI CODES

FIELD	GROUP	SUB-GROUP
06	04	
06	13	

18. SUBJECT TERMS (Continue on reverse if necessary and identify by block number)

RA I; Pichinde virus; Protein Transport; Microcirculation; Water Transport; guinea pigs; arenaviruses; microvascular; shock; hemorrhage; ....

19. ABSTRACT (Continue on reverse if necessary and identify by block number)

These studies complete control observations in Guinea Pig strain 13 in preparation to examine microcirculatory disturbances in Pichinde virus infection. Findings are: Using lymph flux analysis from intestinal mesenteric lymphatics, protein reflection coefficient is .728 ± .018 SEM, and permeability-surface area product is 3.21 ± .29 μl/min/100g. For future studies involving endothelial monolayer transport from infected GP, in vitro new methods demonstrate 1) confluent endothelial monolayers can be assessed functionally from fluorescence intensity patterns of solutes in diffusion chambers, 2) cell morphology is identical to in vivo structure, 3) restricted diffusion develops after three days, and 4) single pore fits to permeabilities are excellent. Using ethane production to mark free radical production, we see 1) it is independent of minute ventilation, 2) is nearly exclusively produced in lung, 3) is inhibited by superoxide dismutase and catalase, 4) is tightly coupled to dietary iron, and 5) and is closely joined to microvascular abnormalities including increased filtration coefficient and lung water. New intravital microscopic methods including infusion of latex beads, have demonstrated: 1) stable images are achieved, 2) mesenteric microvessels normally do not leak dextran, 3) kinetics of Kupffer cell phagocytosis are measurable, and 4) topical tumor necrosis factor results in dextran leaks and blot hemorrhages. This may be important in the splanchnic pathogenesis of hemorrhagic fever.

20. DISTRIBUTION/AVAILABILITY OF ABSTRACT ☐ UNCLASSIFIED/UNLIMITED ☒ SAME AS RPT ☐ DTIC USERS	21 ABSTRACT SECURITY CLASSIFICATION Unclassified
22a. NAME OF RESPONSIBLE INDIVIDUAL Mrs. Virginia M. Miller	22b TELEPHONE (Include Area Code) 301/663-7325	22c OFFICE SYMBOL SGRD-RMI-S

DD Form 1473, JUN 86   Previous editions are obsolete.   SECURITY CLASSIFICATION OF THIS PAGE

AD_____

MICROVASCULAR PHYSIOLOGIC AND ANATOMIC RESPONSES OF THE
GUINEA PIG TO EXPERIMENTAL ARENAVIRUS INFECTION

Midterm Report

Murray A. Katz, M.D.

March 25, 1989

Supported by

U.S. ARMY MEDICAL RESEARCH AND DEVELOPMENT COMMAND
Fort Detrick, Frederick, Maryland   21701-5012

Research Service (151)
Tucson VA Medical Center
Tucson, Arizon   85723

DTIC
ELECTE
APR 2 4 1989
S **H** **D**

DOD DISTRIBUTION STATEMENT

89

FOREWORD

Opinions, interpretations, conclusions and recommendations are those of the author and are not necessarily endorsed by the U.S. Army.

_____ Where copyrighted material is quoted, permission has been obtained to use such material.

_____ Where material from documents designated for limited distribution is quoted, permission has been obtained to use the material.

_mk_ Citations of commercial organizations and trade names in this report do not constitute an official Department of the Army endorsement or approval of the products or services of these organizations.

_mk_ In conducting research using animals, the investigator(s) adhered to the "Guide for the Care and Use of Laboratory Animals," prepared by the Committee on Care and Use of Laboratory Animals of the Institute of Laboratory Animal Resources, National Research Council (NIH Publication No. 86-23, Revised 1985).

_____ For the protection of human subjects, the investigator(s) have adhered to policies of applicable Federal Law 45CFR46.

_____   3/23/89
PI Signature   Date

DTIC
COPY
INSPECTED
4
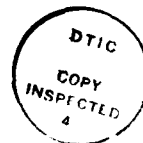
Accession For	
NTIS GRA&I	☑
DTIC TAB	☐
Unannounced	☐
Justification	
By	
Distribution/	
Availability Codes	

Dist	Avail and/or Special
A-1	

TABLE OF CONTENTS

ABSTRACT

These studies complete control observations in Guinea Pig strain 13 in preparation to examine microcirculatory disturbances in Pichindé virus infection. Findings are: Using lymph flux analysis from intestinal mesenteric lymphatics, protein reflection coefficient is .728 ± .018 SEM, and permeability-surface area product is 3.21 ± .29 μl/min/100g. For future studies involving endothelial monolayer transport from infected GP, in vitro new methods demonstrate 1) confluent endothelial monolayers can be assessed functionally from fluorescence intensity patterns of solutes in diffusion chambers, 2) cell morphology is identical to in vivo structure, 3) restricted diffusion develops after three days, and 4) single pore fits to permeabilities are excellent. Using ethane production to mark free radical production, we see 1) it is independent of minute ventilation, 2) is nearly exclusively produced in lung, 3) is inhibited by superoxide dismutase and catalase, 4) is tightly coupled to dietary iron, and 5) and is closely joined to microvascular abnormalities including increased filtration coefficient and lung water. New intravital microscopic methods including infusion of latex beads, have demonstrated: 1) stable images and preparation of mesenteric and hepatic microvasculature are achieved, 2) mesenteric microvessels normally do not leak dextran, 3) kinetics of Kupffer cell phagocytosis are measurable, and 4) topical tumor necrosis factor results in dextran leaks and blot hemorrhages. This may be important in the splanchnic pathogenesis of hemorrhagic fever.

I. Study (a) Characterization of permeability-surface area product (PS) and reflection coefficient (σ) of intestinal microcirculation.

A. Introduction

It has been thought from the Korean experience (1,2) to quite recently (3,4) that hemorrhagic fevers in man and animals are very likely brought about by disruption of the capillary barrier in specified locations. However, more recent studies by Liu and colleagues (5,6) have called this thesis into question and suggest that perhaps interstitial fluid accumulation may result from failure of lymphatic uptake of macromolecules. It therefore is an open question whether permeability is increased, and it remains a critical issue to be settled if one is to understand the mechanism and develop rationales for future definitive therapy in hemorrhagic fevers.

B. Methods

Lymphatic cannulation of prenodal lymphatics is a well described method utilized to assess permeability-surface area products (PS) and reflection coefficients (σ) of a tissue in which there is net filtration by capillaries either in a normal state or induced by partial venous occlusion (for reviews and methods, see 7,8,9). An abbreviated description for the control GP13 study is as follows:

Thirty-eight healthy male GP13s obtained from either ARI (East Bridgewater, Massachusetts) or Crest Caviary (Raymond, California) weighing 643 ± 20.6 SEM grams were anesthetized with 40 mg/kg sodium pentobarbital and tracheotomized. Thirteen were ventilated mechanically, but results did not alter if no ventilator was used. Femoral arterial and venous catheters were placed following which a 200μ/kg bolus of heparin sodium was administered iv following which a variable rate (4-37.5 ml/hr) iv solution of Na 138 mEq/l, K 8mEq/l, HCO$_3$ 28 mEq/l, Cl 118 mEq/l was delivered at 40°C throughout the study. Heparin was added to the infusate to infuse 1μ/kg/minute. The animal's rectal temperature was maintained at 37.5°C on a heating board. A laparotomy was performed, and a polyethylene cannula 8.5 cm long with an id of .38 mm was tied into the main mesenteric lymphatic in the distribution of the superior mesenteric artery. When lymph was seen to flow, the cannula was connected to larger bore PE tubing and the end placed into tared microcentrifuge tubes coated with heparin and layered with water equilibrated mineral oil. Lymph flow rates were computed every half hour with midpoint arterial sampling. Proteins were measured on an autoanalyzer using the biuret method, and for future studies, a limited number of samples were subjected to protein electrophoresis. (These showed a fairly uniform lymph protein distribution for albumin 52-54%, α1 10-11%, α2 18-26%, β 9-13%, γ 3-4%).

Moist umbilical tape was looped around the portal vein and through a segment of Tygon tubing to allow for gentle partial and graded ligation of the portal vein.

Analysis was carried out by the nonlinear crosspoint method described and analyzed previously in our laboratory (9). In brief, if two different lymph flows (L$_1$,L$_2$) are associated with two different lymph/plasma protein concentration ratios (R$_1$,R$_2$), we may write

$$PS = \frac{L_1\,(1-\sigma)}{\ln \dfrac{R_1\sigma}{R_1-(1-\sigma)}} = \frac{L_2\,(1-\sigma)}{\ln \dfrac{R_2\sigma}{R_2-(1-\sigma)}} \qquad \text{Eq 1]}$$

Since the middle and right hand terms are equal, σ may be quickly solved by an iterative root finding routine such as "Quickdraw McGraph" on SuperCalc 4.0 Software. Once σ is known, then PS is explicitly calculated. As described in reference the percent of successful solutions can be quite small owing to random error. Perfect data with random error superimposed can have successful crosspoints in as little as 25% of paired samples (9). Discussion of errors in this method which has been referred to as a "quasi-steady state" method reveals it to be at least as good as most other methods of data analysis (9,10).

C. Results

Twenty-seven guinea pigs (75%) of the group had successful crosspoints for total proteins. Fractionated protein σ and PS values are not included because the electrophoresis studies are not yet completed. There were 268 possible crosspoints in the group of which 56 led to successful computation (20.9%), in fairly good agreement with the percent successes in idealized data (9). Fig 1 shows the histogram for the σ values. The mean was .728 ± .018 SEM with a mode of .85 to .90 and a median value of .740, thus showing little skewness. 70% of the values were within one SD of the mean, and 100% were within two. Fig 2 shows the histogram for PS which had a mean value of 3.21 ± .29 SEM μl/min/100g with a mode from 1.5 to 2.5 and a median of 2.76. Seventy-seven percent of the values were within one SD from the mean and 95% were within two SD. Positive skewness was seen.

D. Discussion

Control guinea pig 13s show a total protein mesenteric circulation σ of .728 ± .018 in a well behaved distribution which though platykurtic appears not different from Gaussian, although a bimodal distribution with peaks at .60-.70 and .85 cannot be ruled out. Protein PS values show a positively skewed distribution with a mean of 3.21 ± .29 μl/min/100g GP. These studies are among the first such direct determinations, and provide the data base against which to compare infected GPs.

II. Study (b) Characterization of GP13 mesenteric microcirculatory module with measurement of microvascular blood flow, granulocyte adherence, and mesenteric local hemorrhage in Pichinde infection.

A. Introduction

Most studies of hemorrhagic fevers' effects on the microcirculation are either done in fixed tissue or by indirect whole organ techniques such as lymph flux analysis. Although such means are important, they do not address the dynamics of capillary effects of the infection at the level of the single capillary or venule in situ. To accomplish this, intravital microscopic techniques are required. These techniques were in large part developed at the University

of Arizona College of Medicine Department of Physiology (11) and are operational in the Benjamin W. Zweifach Microcirculation Laboratories of the Tucson VA Medical Center under the direction of Dr. Robert S. McCuskey, Professor and Head, Department of Anatomy, and Professor of Physiology.

B. Methods

GP13s prepared for surgery as in part I undergo exteriorization of a loop of small bowel whose moistened mesentery is wrapped in saran, suffused with Ringers, and transilluminated on a stage with video taping and either online or offline mapping of the mesenteric module, measurement of erythrocyte velocity, and examination for erythrocyte and dextran leaks and granulocyte adherence. Methods have been discussed in detail elsewhere (12-15).

In brief, optical images are secured using 40 x or 80 x water immersion objectives and appropriate oculars. The resulting microscopic images are televised using a high sensitivity, high resolution silicon vidicon camera or a silicon-intensified target vidicon camera. The televised images are recorded on video tape for subsequent analysis.

Measurement of vessel diameter and blood flow is made either online using an Instruments for Physiology and Medicine (IPM, San Diego) video-shearing monitor and and IPM dual video window or ocular photodiodes coupled to an IPM cross-correlator or from video tapes using IPM video windows and a computerized Bioquant Morphometry System.

For the mesentery, epi-fluorescence of FITC-dextrans of different molecular weights (20-170 kD) are being used to identify changes in microvascular permeability elicited by arenaviral infection.

The quantitative data obtained from the various experiments are evaluated by calculating the mean values for each animal, means ± SEM for each group and subsequently testing for significance between the groups using the Student's t-test. Analysis of variance is used when comparing two groups to control. P<0.05 will be considered significant.

Once the mesenteric microvascular physiology during infection is defined, a variety of therapeutic intervention strategies will be tested. The precise therapies to be tested will depend upon the results obtained above. It is anticipated that they will include inhibitors of the synthesis and/or release of prostaglandins, thromboxane, leukotrienes and cytokines as well as free radical scavengers.

C. Results

Since Studies (b) and (e) utilize the same methods but examine different organ systems, the results are discussed together under Section V C.

D. Discussion

For reasons cited in C., the discussion of Studies (b) and (e) is condensed into Section V D.

III. <u>Study (c)</u> Quantitative assessment of organ involvement by plasma leak and hemorrhage by ^{151}Cr-red blood cells and ^{125}I-human serum albumin leak.

A. Introduction

Studies (a) and (b) examine the gut and mesenteric targets of arenavirus infection, leaving unaddressed the host of other organs which probably are targets as well. It is know that as Hemorrhagic Fever with Renal Syndrome advances in man there is a progression of involvement in a variety of tissues (retroperitoneum, renal medulla, lung) during which some tissues appear to heal as others become involved (1,2). No quantitative measure of this march through the various microcirculatory beds has yet been made, and such a quantitation made during various stages of the disease would be useful in targeting where the significant leaks occur. A benefit of such a search might also be that those organs showing the greatest leaks might subsequently yield endothelial cells for culture in which transport characteristics <u>in vitro</u> may be accurately measured during various stges of infection and therapy. For reasons that infected GP studies are yet to begin, no results from the leak studies exist, and results will thus be presented only from the <u>in vitro</u> work.

B. Methods

1. Blood Volume. Strain 13 guinea pigs will be anesthetized and jugular arterial and venous catheters inserted. Blood volume is measured using radioiodinated (^{125}I) human serum albumin (RIHSA, Mallinckrodt, 1μC/ml) and ^{51}Cr-labelled rat red blood cells (^{51}Cr-RBC; 2μC/ml) using methods previously described by us (16). The amount of free ^{125}I has been determined to be 2% after precipitation of the ^{125}I injectate with 8M trichloroacetic acid. In brief, before injection of radioactive tracers 0.2 ml of blood will be removed from the carotid artery for baseline measurements of radioactivity and hematocrit. The isotopes (0.2 ml of the ^{51}Cr-RBC and 0.25 ml of RIHSA) will be rapidly injected into the jugular venous catheter followed by 0.4 ml of saline. After injection of isotopes, 0.2 ml of arterial blood is removed at 5-min itervals for 30 minutes after clearing the dead space of the catheter. Hematocrit is determined in duplicate and 0.1 ml of blood is added to 2 ml of deionized water for radioactivity counting. The Hct value is multiplied by 0.96 to correct for trapped plasma (17). Blood volume measurements using RIHSA and ^{51}Cr-RBC isotopes are based upon monoexponential extrapolation of the data to zero time.

2. Transvascular Escape Rate. Microvascular permeability to albumin will be measured using the transvascular escape rate of RIHSA (18). Blood RIHSA radioactivity, corrected for unbound radioactivity, is determined at 5-minute intervals for 30 minutes. The transvascular escape rate is calculated from the best single exponential curve fitting of these data points. This best fit is obtained by the method of least squares or a log disappearance curve. The software is a modification of SuperCalc 4.0 to include 95% confidence limits (MAK).

3. Tissue Permeability Measurements. The intensity of permeability changes in each tissue to RIHSA and ^{51}Cr-RBC are determined using a technique similar to the method of Fantone et al. (19). After injection of isotopes at

0 time for blood volume determination, virus-infected and control animals will be observed for one hour without further blood sampling. Five minutes before sacrifice .2 ml of ^{99m}Tc labeled red blood cells will be injected. After this interval a blood sample is obtained, and the animals are sacrificed with intravenous saturated KCl (0.3 ml). The heart (including the thymus) and lungs will be rapidly removed followed by the stomach, small and large intestines, spleen, diaphragm, kidneys, liver, brain and approximately 2g of hindlimb muscle that includes the rectus femoris and the vastus muscle group. These tissues will be gently blotted, weighed and the radioactivity of each sample determined. The tissue permeability index (TPI) will be calculated for both RIHSA and ^{51}Cr-RBC for the venom and control animals as follows:

$$TPI = \frac{^{125}I \text{ or } ^{51}Cr \text{ emissions/min/g tissue weight}}{\text{Average } ^{125}I \text{ or } ^{51}Cr \text{ emissions/min/0.1 ml of blood}}$$

The ^{125}I emissions/min represent the total ^{125}I emissions/min of the tissue minus the percent ^{51}Cr emissions/min of the tissue (average 18.5%) that are counted at the ^{125}I energy level. The above computation is adjusted for tissue content of ^{99m}Tc RBCs which are assumed to remain in the intravascular space over a five-minute period.

    4. Endothelial Cell Culture. Endothelial cells were isolated as described by Ryan, U.S., and Maxwell, G. (20) with minor modifications. In brief, bovine aortas and pulmonary arteries from year old heifers were isolated at a local slaughterhouse, stored in Dulbecco's phosphate buffered saline (PBS; per liter of double deionized water 0.1g $CaCl_2$, 0.2g KCl, 0.2g KH_2PO_4, 0.1g $MgCl_2 \cdot 6H_2O$, 8.0g NaCl, and 2.16g Na_2HPO_4) containing 1X antibiotics (penicillin, 100 U/ml; streptomycin, 100 μg/ml; gentamycin 50 μg/ml) and 3X amphotericin B (0.75 μg/ml), and transported to the laboratory within 30 minutes after collection. After washing with PBS, the vessels were opened under laminar flow conditions and the endothelial cells (EC) removed by gently scraping the intimal surface with a #10 sterile scalpel. The collected cells from each vessel were incubated (37°C) in 0.2% collagenase (collagenase, CLS 2, Worthington Biochemical Co., Freedhold, New Jersey) solution in Hanks' balanced salt solution containing Ca^{++} amd Mg^{++} (HBSS, Gibco) for 20 minutes and centrifuged (5 min, 500g). The cell pellet was mixed with cold HBSS without divalent cations (HBSS free) and centrifuged again. This pellet was vigorously mixed with 5 ml of M-199 growth medium (containing 20% fetal bovine serum, FBS; Hyclone, Sterile Systems, Logan, UT) to break up cell clumps, plated into a T-25 or T-75 flasks (Costar) and incubated at 37°C in 5.6% CO_2 for four hours. After this interval the unattached cells were transferred into a separate flask for 15-20 hours. Growth medium was changed every two days, and each primary culture was carefully evaluated three-four days after explant. At confluence, EC were subcultured 1:3 into T-75 flasks by brief (2 min) exposure to trypsin (0.05%)-EDTA (0.02%, Gibco) at 22°C followed by the addition of growth media. All EC cultures were used before their fourth passage.

    The homogeneity of each EC culture was determined primarily by cell morphology. EC monolayers with a coblestone appearance were tested for uptake of the fluorescent tracer 1,1'-dioctadecyl-3,3,3'3'-tetramethyl indocarbocyanine perchlorate labeled acetylated low density lipoprotein (DIL-acetylated LDL, Biomedical Technologies, Inc., Stoughton, MA) by the fluorescence microscopic

technique of Yoyta et al. (21). In certain instances, detection of this internalized probe with a FACStar fluorescence-activated cell sorter (Becton-Dickinson) was used to separate ECs from contaminating cell types. ECs were also tested for the presence of factor VIII antigen. Sheep anti-human factor VIII related antigen polyclonal antibodies and rabbit anti-sheep IgG tetramethyl rhodamine isothiocyanate conjugate were purchased from Atlantic Antibodies (Scarborough, ME).

5. Monolayer Preparation. Transwell inserts (TW, 0.4μ pore diameter, polycarbonante membrane suports, 6.5mm diameter surface, Costar, Cambridge, MA) were treated with gelatin (Bacto gelatin, Difco Laboratories, Detroit, MI) as described by Postlewaite et al. (22). In brief, sterile TW inserts were heated in a gelatin solution (5 mg/1 of H_2O) to 95°C for one hour in a covered sterile beaker. Each TW was dried under laminar flow conditions, added to a 24-well plate and heated to 85°C for an additional hour. Human fibronectin (25 μg/ml, 50 μl/TW, Collaborative Research) was incubated in gelatin-coated TWs for 30 minutes immediately prior to the addition of cells. Cell cultures were rinsed with HBSS free (5 times) and exposed to trypsin-EDTA (1-2 ml) for 3-4 minutes. After cell detachment 1-2 ml of M-199 with 20% FBS was added, the suspension vigorously pipeted to break up cell clumps and a cell count performed with the aid of a hemacytometer. The fibronectin solution was removed and an EC suspension ($0.5-1 \times 10^6$ EC/ml) was added at supraconfluent ($3-4 \times 10^5$ cells/cm^2) density. After two-four hours the media and unattached cells were removed and replaced with fresh M-199 containing 10% FCS. This solution was changed every two days and the monolayers used at the indicated time intervals. Our filter surface area for exchange (0.33 cm^2) was 15 times smaller than that used by Albelda et al. (23). This small exchange area was selected to limit the number of cells needed for complete monolayer formation. No difference in monolayer formation was detected when filters were coated with gelatin and fibronectin or either material alone.

6. Macromolecular Probes-Analytical Methodology. Fluorescein isothiocyanate-labeled hydroxyethyl starch (FITC-HES) macromolecules have been developed by us as probes of solute exchange (24). The wide range of hydrodynamic radii (>100-<16), globular shape, acidic isoelectric point (pI=4.6) and the constant substitution ratio of FITC to the HES macromolecules regardless of size have prompted the use of these probes to measure size-selective solute transport. FITC-HES probes were size separated on a calibrated high-performance size-exclusion PW 4000 column (Toyo Soda Manufacturing Co., LTD, Tokyo, Japan) using chromatographic (HPSEC) technique and quantitated using a fluorescene spectrophometric-IBM PC computer detection system (24). The advantages of this system in contrast to that recently reported by Albelda et al. (23) are as follows: 1) 25 μl sample volume vs 2 ml; 2) ten minutes vs one day analysis time per sample; 3) muiltiple (3000) analyses without change in the HPSE column calibrations vs 10-20 on Sephacryl S-300 columns; 4) computerized "online" concentration curves vs radiodetection of individual column fractions. The current technique permits the comparison of six concentration curves within one hour and muiltiple size-selective permeability coefficient curves (3-5) are determined on each monolayer.

7. Permeability Determinations. The Transwell (TW, Costar) insert that fits within a chamber of a 24-well plate has been adapted for the diffusion

studies described herein. We performed permeability measurements across 6-12 monolayer preparations per experiment. The top (source) chamber is separated from the bottom (receiving) chamber by a gelatin/fibronectin coated 0.4 μm PC membrane, covered by an endothelial monolayer. Permeability determinations were performed by the addition of 100 μl of FITC-HES (3 mg/ml), RITC-DEX (rhodamine isothiocyanate dextran) (20 mg/ml) or MDPF-(2-methoxy-2,4-diphenyl-3-(2H)-furanone albumin (15 mg/ml) all in M-199 to the top chamber and 600 μl of the same media to the bottom chamber. After a 30-minute equilibration period at 37°C, the media inside the top well was replaced with 37°C media containing tracer. Each bottom well was mixed (withdrawal and immediate return of 200 μl aliquot of media three times) prior to removal of 30 μl sample. Samples from the bottom chamber were removed at 0.5-hour intervals for two or three hours and similar samples were obtained from the top well at two and/or three hours. In this manner, three to five size-selective permeability coefficients can be determined for each monolayer preparation. All permeability experiments showed a substantial macromolecular concentration gradient across each monolayer at the end of a two to three hour experiment.

8. Diffusion, Permeability, and Pore Modeling. The equations described below to determine the size-selective permeability coefficients were used to test for restricted diffusion and pore modeling.

The formulas are based upon Fick's First Law of Diffusion where

$$J_s = -D \cdot f \cdot A \frac{dC}{dx} \qquad \text{Eq 2]}$$

in which D is diffusivity in the biologic or support layer, A is the total area of the layer, f is the fraction of A which is open for solute movement and dC/dx is the concentration gradient at a point x along the interface between the two bulk phases. If V_r and V_s are the receiving and source chamber volumes respectively and C_{tr} and C_{ts} are similarly designated concentrations at time t, $J_s = V_r (dC_{tr}/ds)$ can be substituted into the above equation to yield

$$\frac{V_r \cdot dC_{tr}}{dt} = \frac{DfA (C_{ts} - C_{tr})}{\Delta x} \qquad \text{Eq 3]}$$

Cs is calculated at times other than t=0 by the mass balance relationship that

$$C_{0s} \cdot V_s = C_{ts} \cdot V_s + C_{tr} \cdot V_r \qquad \text{Eq 4]}$$

Finally, since by definition,

$$P \cdot A = D \cdot f \cdot A \frac{}{\Delta x} \qquad \text{Eq 5]}$$

equations 4 and 5 are substituted into Eq 3 which after integration between t1 and t2 and C_{t1r} and C_{t2r} yields the results for permeability

$$P = \frac{\ln\left[\dfrac{c_{0s} - c_{t1r}\,(1+V_r/V_s)}{c_{0s} - c_{t2r}\,(1+V_r/V_s)}\right]}{A \cdot (1/V_r + 1/V_s) \cdot (t_2-t_1)} \qquad \text{Eq 6]}$$

For each experiment P is computed for each molecular size at 0.5, 1, 1.5 and 2 hours with the results meaned. The V terms are changed through sampling at the end of each time period. There are no trends in P measurement over time.

To compute the permeability of the cell layer alone, Pc, from the total permeability (Pt) which is made up of contributions from the cells and the membrane support plus unstirred layer (Ps+us1), we measured Ps+us1 in support material by equation 6 and computed Pc from Pt and Ps+us1 through the series conductance formula:

$$Pc = \frac{Ps+us1 \cdot Pt}{Ps+us1 - Pt} \qquad \text{Eq 7]}$$

a. Testing Pc for restricted diffusion.

Restricted diffusion is the property of a barrier to descriminate molecules by size. This property is thought to characterize the endothelial portion of the capillary barrier. The operational demonstration has its roots in Eq 5 which we divide by A to obtain

$$P = \frac{D \cdot f}{\Delta x} \quad \text{or} \quad \frac{D_0 \cdot f_s}{\Delta x} \qquad \text{Eq 8]}$$

where D and f are the apparent diffusivity of the solute in the layer and f is the open area to total area ratio. D_0 and f_s represent the free diffusivity of solute and fs ($<f$) the open area ratio for the sterically hindered solute. Dividing the above equation by D_0 yields

$$P/D_0 = \frac{f_s}{\Delta x} \quad \text{sometimes written as} \quad \frac{As}{A\,\Delta\,x} \qquad \text{Eq 9]}$$

where As is the channel area available for movement of solute. This may be rewritten

$$P/D_0 = \frac{Ap}{A\,\Delta x} \cdot \frac{As}{Ap} \qquad \text{Eq 10]}$$

where Ap/(AΔx) is a fixed characteristic of the barrier in which Ap/A is the fraction of total area open for point solute or water transport, Δx is mean path length. As/Ap is the area available for solute relative to the open area for point solute or water. The term As/Ap determines the presence or absence of restricted diffusion. As molecular size increases, if RD is present, As/Ap should decrease. Thus for any membrane where (Ap/(AΔx)) is constant, a decrease in As/Ap with molecular radius, a_E, is detected by a corresponding decrease in P/D_0 where P is measured by Eq 6, and D_0 is computed by the Stokes-Einstein equation

$$D_0 = k\ T/(6\pi\eta a_E) \hspace{3cm} \text{Eq 11]}$$

where k is the Boltzmann constant, T is absolute temperature, η is liquid viscosity at T, and a_E is the known molecular radius.

Hence, a plot of P/D_0 vs a_E shows higher values as a_E decreases when restricted diffusion occurs. Any other pattern cannot be used to argue for restricted diffusion.

b. Pore modeling of transport pathways once the diagnosis of restricted diffusion is made.

If P/D_0 vs a_E shows an inverse relationship, diagnostic of restricted diffusion, it is possible to make attempts to fit transport to a right circular cylindrical pore fit, to a slit model, to multiple pores or slits, or to other models of channel geometry such as a fiber-matrix model. In this study we attempted to fit the restricted diffusion positive cell layers to pore or slit models.

For a pore model, As/Ap has a volume steric exclusion term and a center line velocity convective term (7,25) such that if r is the pore radius and $\alpha = a_E/r$, then

$$P = D_0 \cdot \frac{Ap}{A\Delta x} \cdot (1-\alpha)^2(1-2.1044\alpha+2.089\alpha^3-0.948\alpha^5) \hspace{1cm} \text{Eq 12]}$$

For a slit of width = 2w and $\alpha = a_E/w$, the relationship from Curry (26) is

$$P = D_0 \cdot \frac{Ap}{A\Delta x} \cdot (1-\alpha)(1-1.0442\alpha+0.418\alpha^3+0.210\alpha^4-0.1696\alpha^5) \hspace{1cm} \text{Eq 13]}$$

Thus, if P is measured, D_0 is determined and P/D_0 shows an inverse relationship to molecular radius, it may be possible by utilizing least squares minimization fits to Eq 12 or 13 to determine a best fit r or w and $Ap/(A\Delta x)$ for monolayers and seek to determine whether there are anatomic correlates for r or w and their corresponding values of $Ap/(A\Delta x)$ which for pores is (pore number x $\pi r^2/(A\Delta x)$) and for slits is (2w x slit length/$(A\Delta x)$).

9. Scanning and Transmission Electron Microscopy. At the end of each experiment the tracer was removed, the TW was washed with HBSS and the TW fixed with 1/2 strength Karnovsky's fixative for 30 minutes at 4°C. Post-fixation was accomplished with 2% osmium tetroxide for scanning and transmission electron microscopy (EM) using techniques similar to those previously described (27). Endothelial monolayers were, alternatively, fixed with 0.1% ruthenium red in cacodylate/saline buffered 1.1% osmium tetroxide. Scanning EM data were used to assess the percent coverage of each endothelial cell monolayer over the treated polycarbonate membrane. Transmission EM was used to determine the morphology of the endothelium as well as the presence of extracellular matrix.

Monolayers that displayed characteristic FITC-HES distribution profiles in the bottom well for confluent monolayers were selected. (This is discussed under Results, Permeability Studies, Fig 6 below.) Surface area of endothelial

cells as well as the area not covered by cells was determined by morphometry on ten representative scanning EM pictures with the aid of a Bioquant system (Memphis, TN).

10. Statistical Analysis. All data are shown as the mean ± SEM. The 2P<.05 level was selected for statistical significance. A paired Student's t-test (Hewlett-Packard 41CV Stat Pack) was used to compare each test interval from baseline values for selected measurements (28). For the relationship of aged cultures to the presence or absence restricted diffusion, the Fisher Exact Probability Test was done. Pore and slit width computations were carried out by curve fitting routines of P values vs a_E using Equations 12 and 13 above employing Datafit M3.01, Mmorroware, Dynacomp, Austin, TX.

C. Results

Blood volume, transvascular escape rate and tissue permeabilities. No experiments will be performed until virus infected animals are available. However, all labortatory equipment and safety provisions are in effect.

Permeability determinations across endothelial monolayers

Morphology of the Monolayer

Scanning electron microscopic analysis of endothelial cell monolayers exposed to FITC-HES frequently showed what appeared to be a confluent layer of cells. Although the aveage area covered by each cell was 292 ± 16μ^2 with a range of 240-350μ^2 (Fig 3A), small non-confluent interendothelial areas (37 ± 5μ^2) that occurred over 0.6 ± 0.1% of confluent monolayers were seen (Fig 3B). Other monolayer preparations showed a range of uncovered areas up to massive (2500 ± 2000μ^2) holes between cells that occurred in >5% of the filter support (data not shown). Uniform cell attachment during monolayer preparation appeared to be a major factor that led to large gap formation.

Transmission electron microscopy of the endothelial monolayer fre-quently revealed the appearance of a continuous layer of endothelial cells (Fig 4A). Endothelial projections and caveolae that have been shown to be unique ultrastructural features of pulmonary artery endothelium (29) were seen on the endothelial surface (Fig 4A,4B). Although small gaps between endothelial cells were seen (Fig 4B), a variety of cell-to-cell contacts were also noted (Fig 4C,4D,5A,5B). Monolayers treated with ruthenium red showed electron dense sites on the surface of the cell membrane and caveolae that did not appear to extend through the interendothelial cleft (Fig 4B,4C,4D). Other junctions that allowed ruthenium red to penetrate through the junction into the subendothelial space were also seen (Fig 5A). In some instances endothelial cells formed thin cyto-plasmic extensions with the appearance of tight junctions within circuitous interendothelial cell junctions (5B). When monolayers were grown on filter supports for greater than 7 days, double cell layers ("sprouting") were observed. Although extracellular matrix was noted under most endothelial cells, triton X-100 treatment of these monolayers showed many lipid extracted cells attached to the filter. Free extracellular matrix was rarely observed without cell debris, and some filter areas did not show either cells or extracellular matrix (data not shown).

Permeability Studies

FITC-HES chamber concentration profiles predict monolayer confluency

Multiple (3-4) FITC-HES size-selective permeability coefficient (Ps) determinations were made across each monolayer. No predictable trend in the multiple size-selective Ps was noted over the two-three-hour duration of each experiment. Marked variations in size-selective Ps between separate monolayer preparation experiments that ranged by one order of magnitude were observed. In contrast, size-selective Ps across other monolayer preparation experiments showed nearly identical results. The variability of monolayer permeability prompted the development of a functional assay of monolayer confluence. This assay used the size-selective FITC-HES concentration profile of molecules that exchanged across each monolayer at one hour after exposure to this tracer (Fig 6). Curve type 1 was associated with a nearly confluent monolayer (focal holes that represented <1% of the filter surface area). The slow rise in fluorescence intensity (FI) of this curve between 100 to 22 Å molecular radii reflects a "functionally" confluent monolayer. In contrast, curve type 2 that showed a substantial early high molecular radii peak in fluorescence intensity. This chromatogram was associated with a large filter area not covered by cells (>5%). Thus, the FI of the largest FITC-HES macromolecules (first chromatographic peak) relative to the FI of the final peak predicted the "functional" confluence of separate monolayer preparations prior to the completion of each experiment.

Fig 7 depicts the size-selected FITC-HES permeability coefficient (Ps) for gelatin/fibronectin coated 0.4μ pore filters as well as endothelial monolayer covered filters cultured for different periods of time. Significant size-selective resistance to the exchange of FITC-HES across filters seeded with endothelial cells was observed. No trend, however, toward reduced size-selective Ps was seen with the duration of culture. The least permeable of the ten-day-old monolayers showed higher Ps than the least permeable of the three-day-old monolayers. Although all monolayers tested at day ten showed nearly identical Ps, marked variability was noted in Ps for the other groups. Such data suggest that the quality of cell attachment at the time of endothelial cell seeding of each filter is a major determinant of uniform monolayer formation.

A representative experiment of the size-selective Ps for FITC-HES across four-day-old bovine aortic endothelial (BAEC) and epithelial (LLC-PK$_1$) monolayers is depicted in Fig 8. As expected Ps for the epithelial monolayer were below those of endothelial monolayer. However, the curves associated with each monolayer were strickingly different. P for the small (16 Å) FITC-HES probe was restricted to a greater extent than the P for the largest (>100 Å) FITC-HES probe by epithelial in comparison to endothelial monolayers. For example, P for the small probe was reduced by nearly 500% whereas P for the the largest probe declined by 45%. Since these data are similar to those described by Albelda et al. (23), they support the view that decreased monolayer permeability is associated with a shift in the size-selectivity toward much lower Ps for the small probes.

The size-selective Ps of the negatively charged FITC-HES and MDPF-BSA in comparison to neutral RITC-DEX probes across six-day post-primary passaged endothelial cells are shown in Fig 9. Ps for the MDPF-BSA and FITC-HES probes

were not significantly different at 35 Å (3.48 ± 0.33 to 3.70 ± 0.28, P>.05 = not significant). In contrast, P for RITC-DEX at this size was significantly below these values (1.31 ± 0.41, P<.05). In addition, the smaller RITC-DEX macromolecules (<50 Å) were significantly below those of similarly sized FITC-HES. These data show that FITC-HES and MDPF-BSA molecules below 50 Å appeared to permeate endothelial monolayers more than neutral dextrans of similar size.

We tested whether endothelial monolayers showed evidence of restricted diffusion (RD) by dividing the FITC-HES size-selected Ps corrected for unstirred layer and the resistance of the filter by their free diffusion coefficients (D_0) for each molecular size (Fig 10). Restricted diffusion was found in four of 18 three-day endothelial cultures, three of three at ten days and four of four at 17 days. P/D_0 values for endothelial monolayers that showed RD were significantly (P<.001) above those endothelial and epithelial monolayers that did not show this effect. Our "best fit" pore model of each monolayer size-selective permeability coefficient curves that showed restricted diffusion was determined by empirically adjusting our estimates of pore radius and pore area/(path length-total area) ratio. A variety of "best" pore fits were obtained that ranged between 228 and 996 Å with a curve mean of 424 and a median of 361 (Fig 11). For 11 monolayers showing restricted diffusion, the mean r was 445 ± 64 Å and the mean Ap/(AΔx) was 37.0 ± 6.5 cm^{-1} with a mean R^2 of 0.957 ± .008. Fits to a slit model were just as good with the half slit width equal to about half the r. The large SEM for the r fits indicates the insensitivity of the model r to the data. This is expected once the pore diameter exceeds a large enough portion of the mean solute radius. Of course, pore fits (or any other geometric fit) to either the endothelial monolayer size-selective curves that did not show restricted diffusion or to the epithelial monolayer P curves were not possible.

D. Discussion

We studied the size- and charge-selective permeability characteristics of early passaged (<3) cultured bovine aortic and pulmonary artery endothelial cell (EC) monolayers using the anionic tracers, fluorescein isothiocyanate-hydroxyethyl starch (FITC-HES), and 2-methoxy-2,4-diphenyl-3(2H)furanone-bovine serum albumin (MDPF-BSA) in comparison with a more neutral probe, rhodamine isothiocyanate dextran T-500 (RITC-DEX). EC monolayers (1.2x10^5 ECs/Transwell, Costar) were prepared on gelatin/fibronectin treated 0.4μ pore polycarbonate filters and permeability measurements were performed at 3, 6, 10, 17 and 20 days after seeding. Sustantial variations in permeability coefficients (Ps) were noted for many endothelial monolayer preparations. Concentration profiles of FITC-HES probes across the endothelial barrier were used to detect functionally confluent monolayers prior to the end of each experiment. Confluent monolayers showed low MDPF-BSA and FITC-HES Ps that were similar to those previously reported for radiolabeled BSA. These monolayers, however, showed focal holes (37 ± 5μ^2; $\dot{x}$ ± SEM) not covered by endothelial cells that represented <1% of the exchange area. We calculated, however, that this "short-circuit" pathway accounted for <3 percent of all macromolecular exchange. Monolayers cultured on their filter support for >7 days were more than permeable than young (<7 days) endothelial (P<.001) as well as all epithelial monolayers. Similarly, the older (>7 days) more permeable endothelial monolayers showed restricted diffusion of size-selected macromolecular probes. Although confluent monolayers showed no charge selectivity, Ps for MDPF-BSA and the 35 Å FITC-HES probe (3.48 ± 0.33 to

3.70 ± 0.28, P=NS) were significantly above the P for RITC-DEX (1.31 ± 0.41, P<.05) of similar size. These data suggest that older endothelial monolayers display selective barrier function characteristics thought to define the in vivo endothelium.

These studies clearly show that endothelial cell monolayers can be reproducibly shown to exhibit restricted diffusion, a key requirement of the living vascular barrier. With harvesting techniques available to obtain GP13 endothelial cells, a host of future studies become achievable. For example, will Pichinde virus alter macromolecular permeability and selectivity of GP13 endothelial monolayers? Are monocytes necessary? Are soluble factors involved? Can these effects be reversed?

IV. **Study (d)** Assessment of free radical participation in pathogenesis of arenavirus infection by measurement of expired ethane by gas chromatography.

A. **Introduction**

Oxygen free radicals have been demonstrated in a variety of disorders to cause disruption of the microvascular barrier (30). Some evidence exists to support their role in effecting such disruption in Ebola virus infection in rhesus monkeys (31), but no direct measurements have yet been made. This study is designed to track total O_2 free radical production in GP13s infected with Pichinde virus by taking advantage of their nucleophilic attack at the 15 position of lineolinic acid with the production and pulmonary elaboration of ethane gas (32). In rats exposed to air and to 100% O_2, Habib and colleagues have measured a linear rate of production of ethane which is 3.5 to 6.9 times the basal production rate of 5.7 picomoles/min/100g (33). This initial study shows the feasibility of expired ethane in rats (or guinea pigs) as an indication of free radical damage. The questions addressed first were: 1) Since Pichinde infected GPs will likely be tachypneic, is ethane production rate dependent upon minute ventilation? 2) Is the source of expired ethane known? 3) Is ethane production inhibitable? 4) Since free radicals are enhanced by the Fenton reaction which requires a free metal (such as Fe^{++}), does iron homeostasis influence ethane elaboration? 5) Is there a relationship between ethane production or free radical damage and pulmonary capillary hydraulic conductivity-surface area product (K_{fc})?

B. **Methods**

Methods for ethane collection and measurement have been recently published (33). In brief, animals were studied while spontaneously breathing and housed in metabolic chambers that have been previously described. Hydrocarbon free air was directed via teflon tubing into the chambers at a flow rate of 200 ml/min. Inspirate was passed over a cold trap of freshly prepared activated charcoal (vacuum heated at 230°C for one hour) to eliminate all residual ethane from input air. Effluent from the chamber was directed over a second cold trap consisting of a glass cassette containing activated charcoal. After each 30 minutes of collection time, the charcoal in the cassette was poured into a screw top glass test tube of known volume and sealed with a screw top housing a teflon septum. Ethane was liberated from the charcoal by heating at 230°C for five minutes. A known amount of headspace gas was then withdrawn from the

test tube with a precision gas sampling syringe by puncturing the teflon septum and injected onto the column of the chromatograph. The chromatograph contained a 2 meter long 1/4 inch diameter glass column and was packed with Carbosphere 60/80. The chromatograph oven was maintained isothermal at 220°C. Ethane calibration retention time was noted to be 4.74 minutes.

The gas chromatograph responses to known spikes of ethane were linear with a Pearson rank order correlation coefficient of not less than 0.995.

All of the following studies utilized the same method to evaluate questions raised in the introduction.

1st Study - Ethane dependency upon ventilation rate.

12 GP13s were studied after an eight-hour fast. Six of these animals were studied while anesthetized with sodium pentobarbital (3.75 mg/100g) and ventilated via tracheostomies at three different minute ventilations each using a small animal ventilator and a tidal volume of 0.75 ml/100g. Minute ventilation was altered by adjusting the respiratory frequency alone, and each minute ventilation was maintained for at least 90 minutes, enough for three collection periods of 30 minutes at each setting. Arterial blood gases were obtained for measurement of PCO_2 during the second 30 minute ethane sampling period, and intravascular volume was maintained by replacement via this line with a balanced salt solution.

Since animals of different weight have different metabolic rates, PCO_2 should be linearly related to $W^{0.75}/V_E$ (minute ventilation corrected for body weight) where the numerator is animal weight to the 0.75 power and the denominator is minute ventilation. The six other animals were studied while housed in metabolic chambers as discussed elsewhere for rats.

2nd Study - What is the source of ethane during hyperoxia?

Although ethane in the expirate may have its source in many organs other than the lung, ethane is believed to be transported to the blood-air interface from its source and eliminated via the respiratory system. We evaluated the contribution of the lung to the exhaled ethane production by examining exsanguinated rats as well as whole rat lung slices. The rats for this study were not purchased with contract funds, but the equipment used to determine the ethane production was that purchased with contract funds.

Group I consisted of four rats which were anesthetized, tracheostomied and mechanically ventilated. Ethane production rates were determined during mechanical ventilation with hydrocarbon free air (HFA); and the abdominal cavities were opened and aortas transected, thus exsanguinating the animals. Ethane production rates were again measured in this condition, the circulation and thus any return of ethane from organs other than the lung being completely eliminated.

Group II consisted of nine other rats which were anesthetized, mechanically ventilated with HFA and then exsanguinated. Ethane production rates were measured and then 100% oxygen used as the inspirate. Ethane production was measured again.

Five of the animals in Group II were used for Group III. Once ethane production rates on 100% oxygen were determined in these five animals, the inspirate was changed back to HFA and ethane production rates again measured.

Group IV was the control group of six animals which were anesthetized, tracheostomied and ventilated with HFA and then oxygen, ethane production rates being determined during both periods of ventilation. The percent increase in ethane production induced by 100% oxygen ventilation as compared to HFA ventilation was compared to the percent increase in the exsanguinated animals of Group II.

Group V consisted of four rats anesthetized and ventilated as for Group IV. However, once HFA ventilation was initiated, the rats were exsanguinated by aortic section and the lungs removed immediately. Slices from these lungs were incubated in test tubes containing phosphate bufferred saline to which 10mM $FeCl_2$ had been added. Paired samples were placed in tubes whose headspace gas was either 100% oxygen or HFA. After incubation in a shaker bath for 120 minutes, headspace gas was removed for chromatographic ethane analysis and ethane from samples incubated with 100% oxygen were compared to ethane from samples incubated with HFA by paired t-test.

3rd Study - Inhibition of ethane production.

In an attempt to determine that free radicals of oxygen are the determinants of ethane elaboration, we attempted to inhibit ethane production by the use of intratracheal instillation of polyethylene glycol (PEG) conjugated superoxide dismutase and catalase (PEG-SOD and PEG-CAT). Eighteen rats were anesthetized and ventilated with HFA. Either PEG alone (six rats) or PEG-SOD and PEG-CAT (six rats) were instilled down the trachea. Six control animals were ventilated on room air and oxygen and used as control.

4th Study - Role of dietary iron in ethane production.

We have studied the ethane production rates in both homozygotes and heterozygotes of a mouse model of thalassemia that are being supplied by a collaborator, Dr. David Van Wyck. The homozygote thalassemic mice have iron stores four to five times that of the heterozygote mice. Such mice were studied as described above against their heterozygote controls. In addition, their dietary iron was manipulated over a wide range.

5th Study - Connection of ethane production to changes in K_{fc}, lung water, and dynamic compliance.

In an attempt to link the production of ethane, which occurs early in the course of exposure of rat lungs to hyperoxia, to changes in capillary permeability and its subsequent effects, we have initiated studies in isolated perfused rat lungs which can be adapted for use with guinea pigs.

The purpose of these experiments is to demonstrate a link between ethane production and lung capillary permeability changes on exposure to the oxidant H_2O_2. We have established an isolated perfused rat lung after discussion

with various groups who use this model (including the Physiology Department of the University of South Alabama at Mobile). We have chosen to use, as oxidant, H_2O_2 because it is a potent oxidant stimulus, it can be given on either side of the alveolar-capillary membrane, its dose can be easily manipulated and catalase will inactivate it.

Pilot studies on a rat perfused lung model were done to measure K_{fc} of the lung by gravimetric means using methods reviewed elsewhere and familiar to us (34). By elevating venous pressure gradually and measuring the rate of weight gain which is related to filtration, then a K_{fc} can be computed assuming some fixed percent of the venous pressure rise is propagated back to mid capillary. The error in changes in K_{fc} due to errors in estimation of the pressure propagation are quite small (34). In addition to K_{fc}, we have measured wet/dry lung weight ratios and dynamic lung compliance by standard methods. Disturbance in capillary barrier function should increase the former and decrease the latter.

C. Results

1st Study - As predicted, the ventilated animals revealed a linear relationship between PCO_2 and minute ventilation corrected for body weight of the GP13 (Fig 12). Furthermore the ethane production rates for each mechanically ventilated GP13 as calculated from the cumulated ethane production rate during the 90 minute collection period at any specific minute ventilation was found not to correlate in any way with the minute ventilation corrected for body weight for all the animals so studied (Fig 13). Thus minute ventilation is seen not to affect ethane production rate.

The ethane production rate for the mechanically ventilated GP13s over their entire 270 minute ventilation period was calculated neglecting the changes in minute ventilation that were induced (since there was no relationship between minute ventilation and ethane production rate) and compared to the ethane production rate in the six animals whose ethane production rates were measured during spontaneous breathing. As can be seen from Fig 14, there is no difference between ethane production rates in the two groups of animals studied, even though they were examined under completely different conditions.

2nd Study - Fig 15 reveals that ethane production rates in the Group I animals was not changed by exsanguination. Note however, that the standard deviation bar in the circulation intact set of animals is larger than for the exsanguinated group suggesting that some contribution from other organs is a possibility with the circulation intact.

Table 1 reveals that for every animal in group II, ethane production rate increased when the exsanguinated rats were exposed to 100% oxygen. Furthermore, the five animals comprising group III which were ventilated again with HFA all returned toward their initial HFA values for ethane production.

The rats in the control group, Group IV, demonstrated a 381 ± 213 percent increase in ethane production after oxygen was used as the ventilating gas. This value is not statistically different from the percent increase in the ethane production rates found in the exsanguinated animals in Group II (Fig 16).

The _in vitro_ experiments in Group V animals reveal that ethane is produced from the isolated lung alone in substantial quantities and that oxygen increases the ethane liberated significantly (Table 2). The percent increase is $362 \pm 245.5\%$ which is comparable to that seen in the animals of group II.

3rd Study - Table 3 reveals that neither intratracheal instillation of PEG-SOD and PEG-CAT nor PEG alone altered ethane production during HFA ventilation. Compared to normoxic ventilated rats, ethane production increased in the PEG and no treatment groups but not in the PEG-SOD and PEG-CAT groups. Furthermore, the mean increase in ethane production in PEG treated rats was significantly higher than for the no treatment group and for the PEG-SOD and PEG-CAT treated group (Fig 17).

4th Study - Despite the difference in iron stores, ethane production in both groups of mice (iron normal and iron overloaded) demonstrate a linear relationship to dietary iron but not to their phenotype (Table 4) during room air breathing. Furthermore, _in vitro_ rat lung slices in our laboratory produce more ethane when the incubation medium contains iron. Indeed, in one such _in vitro_ study, we found a linear relationship between iron content of the medium and the ethane produced on incubation of lung tissue with oxygen.

5th Study - Pilot studies conducted thus far with this model have indicated that ethane production rates during H_2O_2 exposure increase compared to the saline control. This can be seen in Fig 18. Increased conjugated dienes, another marker of lipid peroxidation, were also found in the lipid extract of lungs exposed to H_2O_2 (Fig 19) along with the increased ethane although we are in the process of improving our method of conjugated diene measurement. Lung water, as measured by wet/dry lung weight ratios was also found to increase as shown in Fig 20. Dynamic lung compliance was predictably decreased, although not as impressively as the increase in wet/dry weight ratios (Fig 21).

Pilot data for the capillary filtration coefficient (K_{fc}) measurements support the hypothesis that capillary leak is caused by the oxidant injury in that K_{fc} was found to increase over the thirty minute period during which it was measured. As demonstrated in Table 5, the capillary filtration coefficient thirty minutes into the isolated perfused rat lung experiment is less in the saline control experiments as compared to the H_2O_2 experiments.

D. Discussion

Study 1 demonstrates that the elimination rate for ethane is not dependent on minute ventilation and is constant in resting normal GP13. This is analogous to the production and elimination of CO_2 by animals in which the gas is neither metabolized nor stored and diffuses rapidly into the alveolar space.

These data should simplify the measurement of ethane production rate in guinea pigs having different minute ventilations (such a sick versus healthy animals) since changes in minute ventilation appear not to alter ethane production rates.

Study 2 - Although other organs have been shown to produce ethane, we have demonstrated not only that the lung itself can produce substantial quantities of the hydrocarbon but that it is probably the major source of ethane when animals are ventilated with 100% oxygen. This provides a direct test for pulmonary free radical production in infected GP13s.

Study 3 - These data suggest that oxygen metabolites contribute to the ethane production in rats exposed to 100% oxygen and that PEG alone increases the effect of oxygen on ethane production. PEG-SOD/CAT decrease free radical metabolites induced by hyperoxia.

Despite the current popularity of PEG bound scavengers to treat free radical excess, these studies indicate caution is necessary in interpretation, since PEG alone enhances ethane production.

Study 4 - The status of iron in the diet is important in potentiating free radial production and presumably free radical damage. This brings to mind an intriguing possibility: Since hemorrhagic fever is common outside the United States, and since world wide foodstuffs provided by western countries are usually iron fortified, is there a relationship between dietary iron and clinical susceptibility to hemorrhagic fever? Dietary studies in infected GP13s should be able to address this question.

Study 5 - Measurement of dynamic lung compliance has not revealed the same degree of change as was seen in the wet/dry ratios. This probably reflects the need for substantial changes in lung water to result in a diminution in dynamic compliance, but the data shown in Fig 21 suggest that the trend in the H_2O_2 treated animals is towards a reduction in dynamic compliance compared to the saline control.

The methods can be adapted to isolated perfused guinea pig lungs infected or not with the Pichinde virus. Thus, assessment of K_{fc}, lung water, and dynamic lung compliance at various stages of the disease process can be determined to clarify the changes the virus induces on lung capillary permeability, a change that is supposed to occur late in the disease course.

V. Study (e) Morphometric and intravital assessment of hepatic microcirculation and Kupffer cell function.

A. Introduction

Since macrophages are a major target in lethal arenavirus infection, and hepatic necrosis is also a feature (3,35,36), this study is designed to investigate both features simultaneously in the living hepatic microcirculation in control and infected GP13s.

Hepatic microvascular failure is implicated in the pathophysiology of septic and endotoxic shock; and, Kupffer cells which comprise one of the hepatic sinusoidal lining cells are not only phagocytes but also the source of a variety of toxic and beneficial mediators such as prostaglandins, leukotrienes, thromboxanes, free radicals, interleukin-1, tumor necrosis factor, interferon, lysosomal enzymes, procoagulants, etc. (reviewed in references 37-41). As a result,

these cells have been implicated in playing a major role in septic and endotoxic shock since bacterial endotoxin which is principally cleared by Kupffer cells also modulates the release of these substances (39-41). This is of particular interest since macrophages are reported to a major target for arenavirus infection; and, Kupffer cell hyperplasia and hepatic necrosis are frequently observed (3). This suggests that involvement of the hepatic microvasculature and Kupffer cells in the pathophysiology of arenaviral infections may contribute significantly to the lethality of the disease.

Given the above, the purpose of the current investigtion is to elucidate the dynamic events that occur in the hepatic microvasculature during the lethal course of an animal model of human arenavirus infection which employs Pichinde viral infection of strain 13 guinea pigs. In addition, as noted in Section II, the mesenteric microvasculature also is being studied and the responses compared and contrasted to those in the hepatic microvasculature. The mesentery provides a convenient site to evaluate the effects of arenaviral infection in a relatively simple microvascular bed containing arterioles, capillaries having continuous endothelium and basal lamina, and venules. In contrast, the highly metabolic liver has a highly complex microvasculature containing sinusoids having a dual afferent blood supply from the portal venule and hepatic arteriole. The sinusoids have fenestrated endothelial walls and are not surrounded by a continuous basal lamina; they also contain the phagocytic Kupffer cells on their luminal surfaces. Such microcirculatory studies are best done using a high resolution _in vivo_ microscopic method so that the direction and magnitude of dynamic microvascular events can be assessed in life as a function of time. Subsequent electron microscopic evaluation permits ultrastructural evaluation of cellular damage. These studies should be useful in elucidating the pathophysiology of this disease and in developing a strategy for therapeutic intervention.

As a result, the specific aims of this project are to determine qualitatively and quantitatively what alterations occur as a function of time in the hepatic and mesenteric microvasculature in strain 13 guinea pigs following infection with Pichinde virus. Changes in the patterns, pathways, rates and volumes of blood flow through the hepatic microvasculature are assessed by high resolution light microscopy of the liver and mesentery _in situ_ in anesthetized animals. The causes of these changes, e.g., vasodilation or constriction, endothelial adhesion of leukocyte and platelets and/or intravascular aggregation, sinusoidal lining cell swelling and/or rupture, etc., will be determined. Alterations in phagocytic Kupffer cell function in the liver also will be quantitatively assessed. Subsequently, the ultrastructural alterations in the microvascular wall will be elevated by transmission and scanning electron microscopy. Once the hepatic microvascular pathophysiology is defined therapeutic intervention strategies will be tested, e.g., inhibitors of the synthesis and/or release of eicosanoids, cytokines as well as free radical scavengers, Ribavirin (42), interferon (43), etc.

B. **Methods**

Strain 13 guinea pigs (300-500g) innoculated with 10^4 plaque forming units of Pichinde virus adapted by USAMRIID for 14-day lethality will be the experimental model of arenavirus infection. Groups of six animals will be

studied on even days from 0 to 14 days after infection. Uninfected animals are currently being studied for controls.

The livers (and mesenteries) are studied by high resolution, in vivo microscopic methods (37,38). To accomplish this, a lobe of the liver (or a loop of small intestine) is gently exteriorized through an incision in the abdominal wall, and transilluminated or epi-illuminated with monochromatic light. Homeostasis will be maintained by suffusion of the exposed liver with Ringer's solution warmed to body temperature. Televised images then are recorded on video tape for subsequent analysis.

The function of individual Kupffer cells is assessed by measuring the rate of phagocytosis of individual FITC-latex particles (0.8 μm in diameter) injected intraportally (mesenteric vein). This is determined by measuring the time required for individual Kupffer cells to internalize single particles once they have contacted the cell surface (40,41,44-46). Such measurements are made in the periportal (Zone 1), midlobular (Zone 2), and centrilobular (Zone 3) areas of each liver. Ten measurements are made in each area. The distribution and relative number of phatocytic Kupffer cells also is measured by counting the number of cells that phagocytose latex. This is done 15 minutes after infusing a standardized concentration of latex particles (0.8μ in diameter). To assess regional distribution, the number of phagocytic Kupffer cells per standardized microscopic field is counted in 10 periportal (Zone 1), 10 midlobular (Zone 2), and 10 centrilobular (Zone 3) regions. For these measurements the livers are imaged by incident fluorescence microscopy (37,38). This permits the use of lower magnifications (40 x objective) and subsequently larger fields of measurement. While 1.0 μm latex particles are easily visualized with an 80 x objective, they are difficult to see with the 40 x objective unless fluorescence microscopy is used. However, the field of measurement with the 80 x objective is quite restricted and best used to evaluate phagocytosis of single particles by individual Kupffer cells.

In addition to the above evaluation of Kupffer cell (KC) function, the following hepatic microvascular parameters are assessed: (a) patterns of blood flow within the lobules and velocites of blood flow in the sinusoids; (b) aggregation and/or adhesion of formed elements in the blood to each other or to the sinusoid walls; and (c) dimensional changes in the microvasculature due to constriction, dilation and/or swelling or sinusoidal lining cells. The relative adequacy of blood perfusion through the sinusoids is evaluated by counting the number of sinusoids containing flow in the same microscopic fields where the number of phagocytic KC was previously determined. Similar parameters are evaluated for the mesenteric microvasculature.

The ultrastructural changes that occur in the liver and during the course of the disease will be evaluated by routine transmission and scanning electron microscopic methods (47,48). For these studies, groups of three animals will be used with a group sacrificed on even days 0 to 14 days following innoculation. The observed ultrastructural changes will be correlated with thsoe recorded by in vivo light microscopy. Particular attention will be paid to damage to the hepatic sinusoid wall including endothelial cells and their fenestrae, Kupffer cells and perisinusoiudal fat-storing cells of Ito. In the

mesentery, attention will be paid to alteration on the integrity of capillary venules, particularly their endothelial junctions and basal laminae.

Once the hepatic (and mesenteric) microvascular physiology is defined a variety of therapeutic intervention strategies will be tested. Quantitative data which are normally distributed will be compared using standard ANOVA. Ordinal data or nonnormally distributed information will be compared between groups and/or times by the Mann-Whitney U test, Friedman two-way ANOVA, and possibly the Kendall rank correlation test. All of these are in use in our laboratories.

C. Results for Studies (b) and (e) Together

Until very recently it has not been possible for us to study the effects of arenavirus on the microcirculation due, first, to a lack of appropriate containment facilities; and, second and most recently, a shortage of strain 13 guinea pigs. As a result, during the first 18 months of this project efforts have been directed toward establishing reproducible methodologies to study the guinea pig mesenteric and hepatic microvasculature by high resolution in vivo microscopy. It was found that many modifications in our instrumentation were required to accommodate guinea pigs; the equipment in the past was designed for use primarily with mice and small rats.

First, in order to facilitate capture and enable analysis of microcirculatory images derived from the in vivo microscope, several key pieces of electronic equipment were installed and/or tested. These include the Metrobyte data acquisition equipment and Bioquant morphometric hardware, as well as the associated software to interface them with the PCAT. This equipment provides the means to acquire the qualitative fluorescence data needed to determine permeability from the video images of mesentery and liver. Several tests were performed to check system sensitivity and to calibrate this equipment. A number of miscellaneous but important equipment modifications and software tests were also done to complete equipment installations.

Secondly, a new microscope stage was designed and built to study the guinea pig mesentery. Several improvements were made that dramatically enhanced our ability to visualize and maintain the mesenteric preparation during experiments (see Fig 22). Based on this design another stage was designed and built for liver preparations, since the stage used for rat liver was not adequate for the guinea pig. A second revision of this design still is required and currently is being designed and constructed. Nevertheless, a number of adequate images of the liver have been recorded including phagocytosis of fluorescent latex particles by the Kupffer cells (Fig 23).

After the new stage was built and tested a number of mesenteric preparations were examined mostly using 150 kD molecular weight FITC-labelled dextrans. Initially, the FITC-dextrans were injected as a single bolus into a penile vein (0.3-0.4 ml, 10% w/v). This bolus was used to determine the time to reach a steady-state fluorescence intensity in the cell-free plasma layer of the mesenteric microvessels as well as a preliminary estimate of the fluorescence intensity in the extravascular space. This information is necessary to determine an estimate for microvascular permeability (P) of the FITC-dextrans. Although

models to determine values for P are not presently developed, image analysis indicates that very little of the 150 kD FITC-dextrans are extravasated (see Figs 22,24). Histamine was given either systemically (or topically) after a steady-state concentration was reached to determine if microvascular leakage of dextrans could be obtained. While leakage spots have been observed in post-capillary venules of the hamster cheek pouch our preliminary results for the guinea pig do not clearly show that this phenomenon occurs in the mesentery. However, there is an indication that small leakage sites may be located near some peri-vascular cells and in the proximity of venular bifurcations. No apparent difference between mode of administration was found. More recent work using topically applied recombinant human tumor necrosis factor (TNF) to the GP mesentery demonstrated venular leakage of 150 kD FITC-dextran, as well as frank blot hemorrhages (see Fig 25).

The use of 70 kD molecular weight FITC dextran was initiated to evaluate whether this smaller size molecule penetrated the microvascular wall under normal (healthy) conditions. Qualitatively, little penetration was observed, and the result appeared similar to those seen for 150 kD FITC dextran. Qualitative computerized image analysis continues to be in progress. Studies of smaller FITC dextran (10-20 kD) recently have been initiated but with limited results to date.

Quantification of transport and uptake of the FITC-dextrans by hepato-cytes has not been possible because the redesigned stage still is not adequate and revision has not yet been completed. Attempts to use the smaller stage available for rat livers have met with only limited success. However, a few good observations have provided some useful information that has permitted us to make modifications to procedures used for the guinea pig experiments. First, the dose (obtained from literature) of FITC-dextrans injected appears to be too high, since it significantly affects liver hemodynamics, mainly by reducing blood flow and causing liver congestion. Lowering the total mass injected has improved this situation. Secondly, using steady-state concentrations of FITC-dextrans to analyze permeability for liver does not appear to be satisfactory. The protocols are being modified to use either pulses injected into the portal vein or systemic circulation before the mesentery is studied in the same preparation.

Pulse injections of the FITC-dextrans, in contrast to a steady-state concentration, are being evaluated. This approach has the potential to eliminate the high circulating levels of FITC-dextrans which appear to cause liver conges-tion and to permit repeated measurements of permeability at the same sites (more consistent with presently developed models). In addition, we are attempting to develop a methodology to inject pulses of FITC-dextrans locally; that is, in close proximity to the mesenteric loop exteriorized for observation on the microscope stage. Special small diameter catheters and attached needles were secured to aid in this process.

Finally, for in vivo studies it has been determined that smaller (young adult) guinea pigs (250 gms) should be used in order to provide sufficient observation time for each experiment. Microvascular flow is better maintained using this size animal, and the guinea pigs seem to better tolerate the initial and maintenance doses of sodium pentobarbital. This provides much better images of the liver and the mesentery.

D. Discussion of Studies (b) and (e) Together

A number of protocols and procedures related to the animal size, surgery, anesthestic administration, FITC-dextran concentation, and drug doses have been established to permit study of livers and mesentery in control of guinea pigs as well as animals infected with arenavirus. Electron microscopic evaluations of the hepatic and mesenteric microvasculature are in progress as are in vivo microscopic evaluations of Kupffer cell phagocytic activity.

References

1. Giles RB, Sheedy JA, Ekman CN (1954) The sequellae of epidemic hemorrhagic fever. Am J Med 16:629-638

2. Lukes RJ (1954) The pathology of thirty-nine fatal cases of epidemic hemorrhagic fever. Am J Med 16:639-653

3. Peters CJ (1984) Arenaviruses, Ch19, in Textbook of Human Virology (ed RB Belshe), pp 513-545, PSG, Littleton

4. Peters CJ, Johnson KM (1984) Hemorrhagic fever viruses, Ch44, in Concepts in Viral Pathogenesis (eds AL Notkins, MBA Oldstone), pp 325-337, Springer-Verlag, New York

5. Pinter GG, Liu CT, Peters CJ (1988) Capillary permeability to labelled albumin and cervical hemodynamics in Pichinde virus-infected strain 13 guinea pigs. FASEB J 2:A1524 (Abstr)

6. Liu CT, Pinter GG (1989) Transport of ^{125}I-albumin from interstitium of soft palate and peritoneum to cervical lymphatics and plasma in Pichinde virus-infected strain 13 guinea pigs. Report on Contract DAAL03-86-D-001, Feb 15

7. Katz MA (1982) System analysis of vascular membrane water and protein transport: general method and application to canine hindquarters. Microvasc Res 23:31-55

8. Katz MA, Starr JF (1984) Effects of acetylcholine on peripheral vascular protein permeability. Lymphology 17:28-33

9. Katz MA (1985) Comparison of crosspoint and least-squares regression methods in computation of membrane protein flux parameters from lymph flux analysis. Microvasc Res 30:207-221

10. Katz MA New formulation of water and macromolecular flux which corrects for non-ideality: theory and derivation, predictions, and experimental results. J Theor Biol 112:369-401

11. Johnson PC, Wayland H (1967) Regulation of blood flow in single capillaries. Am J Physiol 212:1405-1415

12. McCuskey RS (1981) In vivo microscopy of internal organs. Prog Clin Biol Res 59:79-87

13. Stauber WT, Ong S, McCuskey RS (1981) Selective extravascular escape of albumin into the cerebral cortex of the diabetic rat. Diabetes 30:500-503

14. Fagrell B, Fronek A, Intaglietta MA (1977) Microscope television system for studying flow velocity in human skin capillaries. Am J Physiol 233:H318-H321

15. Koo A (1984) Current methods and concepts on the visceral microcirculation in Progress in Applied Microcirculation (eds K Messmer, F Hammersen), pp 54-68, Karger, Basel

16. Schaeffer RC Jr, Chilton S-M, Carlson RW (1985) Puffadder venom shock: a model of increased vascular permeability. J Pharmacol Exp Ther 233:312-317

17. McGovern JJ, Jones AR, Steinberg AG (1955) The hematocrit of capillary blood. New Engl J Med 253:308-312

18. Parving HH, Rossing N (1973) Simultaneous determination of the transvascular escape rate of albumin and IgG in normal and long term juvenile diabetic subjects. Scand J Clin Lab Invest 32:239-244

19. Fantone JE, Schrier D, Weingarten B (1982) Inhibition of vascular permeability changes in rats by captopril. J Clin Invest 69:1207-1211

20. Ryan US, Maxwell G (1986) Microcarrier cultures of endothelial cells. J Tiss Cult Meth 10:7-8

21. Voyta JC, Via DP, Butterfield CE, Zetter BR (1984) Identification and isolation of endothelial cells based upon their increased uptake of acetylated-low density lipoprotein. J Cell Biol 99:2034-2040

22. Postlewaite AE, Snyderman R, Ryan D (1976) The chemotactic attraction of human fibroblasts to a lymphocyte-derived factor. J Exp Med 144:1188-1203

23. Albelda SM, Sampson PM, Haselton FR, et al (1988) Permeability characteristics of cultured endothelial cell monolayers. J Appl Physiol 64:308-322

24. Schaeffer RC Jr, Renkiewicz RR, Chilton S-M, et al (1986) Preparation and high-performance size-exclusion chromatographic analysis of fluorescein isothiocyanate-hydroxy ethyl starch: macromolecular probes of the blood-lymph barrier. Microvasc Res 32:230-243

25. Faxen H (1959) About T. Bolin's paper: on the drag of rigid spheres moving in a viscous liquid inside cylindrical tubes. Kolloid Z 167:146

26. Curry F-R E (1974) A hydrodynamic description of the osmotic reflection coefficient with application to the pore theory of transcapillary exchange. Microvasc Res 8:236-252

27. Schaeffer RC Jr, Barnhart MI, Carlson RW (1987) Pulmonary fibrin deposition and increased permeability to protein following microthromboembolism in dogs: a structure-function relationship. Microvasc Res 33:327-352

28. Wallenstein S, Zucker CL, Fleiss JL (1980) Some statistical methods useful in circulation research. Circ Res 47:1-2

29. Smith U, Ryan JW (1973) Electron microscopy of endothelial and epithelial components of the lung: correlations of structure and function. Fed Proc 32:1957-1966

30. Katz MA (1986) The expanding role of oxygen free radicals in clinical medicine. West J Med 144:441-446

31. Fisher-Hoch SP, Platt GS, Weild GH, et al (1985) Pathophysiology of shock and hemorrhage in a fulminent viral infection (Ebola). J Infect Dis 152:887-894

32. Reilly CA, Cohen G (1974) Ethane evolution: a new index of lipid peroxidation. Science 183:208-210

33. Habib MP, Eskelson C, Katz MA (1988) Ethane production rate in rats exposed to high oxygen concentration. Am Review Resp Dis 137:341-344

34. Katz MA (1977) Capillary filtration measurement by strain gauge: I. Analysis of methods. Am J Physiol 232:H354-H360

35. Lewis RM, Cosgriff TM, Peters CJ, Morril JC (1987) Differentiation of a human monocytic cell line associated with increased production of Rift Valley fever virus by infected cells. J Med Virol 23:207-215

36. Tandon BN, Acharya SK (1987) Viral diseases involving the liver. Baillieres Clin Gastroent 1:211-230

37. McCuskey RS (1983) The hepatic microvascular system. In Microcirculation of the Alimentary Tract (eds A Koo, SK Lam, LH Smaje), pp 57-68, World Sci Publ Co, Singapore

38. McCuskey RS, McCuskey PA, Mitchell DB, et al (1986) Ultrastructure of the canine hepatic sinusoid. In Cells of the Hepatic Sinusoids I. (eds A Kirn, DL Knook, E Wisse), pp 509-510, Kupffer Cell Foundation, Leiden

39. McCuskey RS, Urbaschek R, McCuskey PA, Urbaschek B (1982) In vivo microscopic responses of the liver to endotoxins. Klin Wochenschr 60:749-751

40. McCuskey RS (1986) Hepatic microvascular dysfunction during sepsis and endotoxemia. In: Cytoprotection and Cytobiology, Vol. III (ed M Tsuchiya), pp 3-17, Excerpta Medica, Amsterdam

41. McCuskey RS, McCuskey PA, Urbaschek R, Urbaschek B (1987) Kupffer cell function in host defense. Rev Infect Dis 9:S616-S619

42. Remesar MC, Blejer JL, Weissenbacher MC, Nejamkis MR (1988) Ribavirin effect on experimental Junin virus-induced encephalitis. J Med Virol 26:79-84

43. Dejean CB, Ayerra BL, Teyssie AR (1987) Interferon response in the guinea pig infected with Junin virus. J Med Virol 23:83-91

44. Reilly FD, Dimlich RVW, Cilento EV, McCuskey RS (1983) Hepatic microvascular regulatory mechanisms. III Aminergic mechanisms as related to mast cells. Microcircul Clin Exp 2:61-73

45. McCuskey RS, Urbaschek R, McCuskey PA, et al (1984) Deficient hepatic phagocytosis and lysosomal enzymes in the low endotoxin-responder, C3H/HeJ mouse. J Leukocyte Biol 36:591-600

46. McCuskey RS (1986) "In vivo" microscopy of organs. In: The Science of Biological Specimen Preparation: 1985 (eds M Muller, R Becker, A Boyde, JJ Wolosewick), pp 73-77, SEM Inc, Chicago

47. McCuskey RS, Urbaschek R, McCuskey PA, Urbaschek B (1983) In vivo microscopic observations of the responses of Kupffer cells and the hepatic microcirculation to Mycobacterium bovis BCG alone and in combination with endotoxin. Infect Immunity 42:362-367

48. McCuskey RS, McCuskey PA, Urbaschek R, Urbaschek B (1984) Species differences in Kupffer cells and endotoxin sensitivity. Infect Immunity 45:278-280

Table 1

Picomoles of Ethana Production Rates in Exsanguinated,
Ventilated Animals[1] During Ninety Minute Exposures to Hydrocarbon
Free Air (HFA) or 100% Oxygen.

Rat	HFA	Oxygen	HFA
1	5.05	7.55	–
2	3.32	7.03	–
3	2.05	8.44	–
4	3.22	8.98	–
5	1.47	45.74	1.02
6	2.55	56.92	6.65
7	.233	2.42	1.72
8	.67	2.17	.60
9	1.03	7.28	1.65
Mean ± SD	0.18 ± 1.53	16.28 ± 20.21	2.33 ± 2.46

1. Ethane production in picomoles/min/100gm rat.

Table 2

Picomoles of Ethane Produced _in vitro_ per Gram of Wet Lung
Tissue With Headspace Gas Hydrocarbon Free air (HFA) or Oxygen [1].

Rat	HFA time 120 min	Oxygen time 120 min
A	4.76	17.75
B	3.71	15.42
C	1.90	15.48
D	5.56	13.73
Mean ± SD	3.98 ± 1.50	15.60 ± 1.65*

* Significantly different from HFA (2P<0.005).

1. Tissues incubated in a shaker bath at 37°C for 120 minutes
in phosphate buffered saline containing 10mM $FeCl_2$.

Table 3

Treatment (N)			Normoxia	Hyperoxia
None (6)			0.99 ± 0.35	4.24 ± 0.89
	pre	post		
PEG (6)	2.48 ± 0.48	2.72 ± .76		16.33 ± 9.98
PEG-SOD/CAT (6)	2.24 ± 1.37	1.95 ± .64		4.09 ± 2.04

Values in pm/min/100g ± SD

Pre and Post PEG or PEG-SOD/CAT values for ethane production while venti-
lated with hydrocarbon free air were not different. Oxygen caused an
increase in all values of ethane production but the greatest effect was in
the PEG only treated animals.

Table 4

Cellular Iron Toxicity: Effect of Thalassemia and Food Iron Fortification

Effect of Phenotype and Dietary Iron on Ethane Production (pm/100g/min)

Phenotype	Dietary	Iron	(mg/g)		Effect of Diet
	0.00	.30	.6	3.0	
Homozygotes mean	7.7	10.4	13.4	20.1	
sd		.7	.0	.4	
Heterozygote mean	6.4	11.8	13.8	15.8	P<.001
Controls sd		.6	.3	.1	

Effect of Phenotype P=.181
(iron-free diet groups have not yet been completed)

Table 5

Effect on capillary filtration coefficient [1] (Kfc) thirty minutes after H202 administration in the isolated perfused rat lung (mean ± SD).

Saline *	H202*
0.17 ± 0.173	2.81 ± 3.7

*Three animals in each group.

1. ml/min/cm H20/100 gm lung.

Figure Legends

1. Histogram of σ values for 27 guinea pigs resulting in 56 successful computations. 70% of the values were within one SD from the mean and 100% were within two SD.

2. Histogram of PS values for 27 guinea pigs resulting in 56 successful computations. The mode of 1.5 to 2.5 and the median of 2.76 were less than the mean of 3.21 showing positive skewness. Nonetheless, 77% of the values were within one SD from the mean and 95% were within two SD.

3. Scanning electron micrographs of a confluent bovine aortic endothelial cell monolayer. Panel A shows the uneven features of a single cell with confluent interendothelial junctions with other endothelial cells. Panel B shows an apparent confluent monolayer with certain small holes where endothelial cells do not cover the polycarbonate (PC) filter (arrow indicates open pores of PC filter).

4. Thin transmission electron micrographs of primary passaged bovine pulmonary artery endothelial cell monolayer grown on gelatin/fibronectin-coated 0.4μ polycarbonate membrane for 4 days. Panel A shows a low power view of an endothelial monolayer. An endothelial cell projection is evident (arrow). No extracellular matrix is seen under the monolayer. Panel B shows an area with no connection between cells and which provides ruthenium red direct access to the PC filter. Caveoli are noted to contain ruthenium red (arrow). Panels C and D show two junctions that appear to exclude ruthenium red while there is marked binding of this material onto the endothelial glycocalyx. Bars indicate respective distance in μm (μ).

5. Transmission micrographs of primary passaged bovine pulmonary artery and aortic endothelial cell monolayers grown on a gelatin/fibronectin-coated 0.4 polycarbonate membrane for 4 days. Panel A shows dense ruthenium binding to the endothelial luminal surface that extends into an interendothelial cell junction. Substantially smaller amounts of this material are seen bound to the abluminal cell surface (arrow). Panel B shows a complex aortic interendothelial cell junction not exposed to ruthenium red. The attenuated endothelial membranes form a circuitous pathway with the appearance of a tight junction.

6. Size-selective passage of FITC-HES across confluent (curve 1) and non-confluent (curve 2) endothelial monolayers. Fluorescence intensity of size-selected FITC-HES plotted as a function of molecular radius (Å) for bottom chamber samples obtained one hour after the addition of FITC-HES to the top well. Each curve type was correlated with endothelial cell monolayer confluency by scanning electron microscopy. The mean percent membrane area uncovered (depicted to the right of each curve) was determined by morphometry.

7. Size-selectivity of FITC-HES after selected period of monolayer culture. Permeability coefficients plotted as a function of molecular radius for FITC-HES macromolecules across the "best" (least permeable) endothelial cell monolayers at 3, 10, 17 and 20 days after cell plating are shown. The size-selected permeability coefficients for a gelatin/fibronectin-coated filter support containing no cells is also depicted.

8. Size-selectivity of FITC-HES across an endothelial monolayer in comparison to an epithelial (LLC-PK$_1$) monolayer. Permeability coefficients plotted as a function of molecular radius for FITC-HES macromolecules across a representative bovine aortic endothelial cell monolayer (BAEC) at 6 days in comparison to an epithelial cell (LLC-PK$_1$) monolayer are shown.

9. Comparison of FITC-HES, MDPF-BSA and RITC-DEX across bovine aortic endothelial monolayers 6 days after monolayer preparation. Size-selective permeability coefficients for each probe plotted as a function of molecular radius show that the 35Å FITC-HES probe and MDPF-BSA display similar monolayer restriction. RITC-DEX, however, is significantly (noted by stars) below these coefficients for all intermediately sized molecules (< 50Å).

10. Restricted diffusion test of endothelial and epithelial monolayers. Restricted diffusion is determined by dividing the permeability coefficient (P) by the calculated free diffusion coefficients (D$_0$) for each size-selected FITC-HES probe plotted as a function of molecular radius. The flat P/D$_0$ values for young endothelial cells (3 day) (open circles) was significantly different from the classic restricted diffusion curve shown by the older endothelial cells (10-17 day) (closed circles) ($p<.025$). The younger cells showed no restricted diffusion. The epithelial cells (open triangles) showed the lowest permeabilities and no evidence of restricted diffusion over this solute range.

11. Single pore model of endothelial monolayers that displayed restricted diffusion. A "best-fit" of computer-generated single pore model to predict the mean permeability coefficients plotted as a function of molecular radius (a$_E$) is shown. Note that endothelial monolayers with low Ps as well as the Ps seen with epithelial monolayers could not be fit to any pore model.

12. Arterial PCO$_2$ versus minute ventilation corrected for metabolic activity. Only five GP 13 are used since the arterial line in one animal did not function. As predicted, PCO$_2$ is directly related to metabolic activity thus demonstrating the adequacy of measurement techniques.

13. Scattergram of ethane production rate versus minute ventilation corrected for metabolic rate for all minute ventilations in all GP13s. No correlation is seen. Asterisks identify the outliers.

14. Comparison of cumulated ethane production in 6 spontaneously breathing GP13 with the six mechanically ventilated animals, ignoring the minute ventilation changes that were induced. The rates were the same.

15. Ethane production rates for exsanguinated animals and animals with circulation intact. The values were not different. Differences in variances between groups leaves open the possibility of extrapulmonary sources of ethane in intact animals.

16. Percent change in ethane production on exposure to 100% oxygen in exsanguinated animals and in control animals. The values are not different.

17. Absolute change in ethane production rates on exposure to 100% oxygen after hydrocarbon free air ventilation in animals treated intratracheally with either polyethylene glycol alone (PEG) or PEG attached to superoxide dismutase or

catalase (PEG-SOD/CAT) or control. PEG induces ethane production, but PEG-SOD/CAT reduces it.

18. Lung conjugated dienes measured spectrophotometrically at 232 nM in isolated perfused rat lungs instilled intratracheally with either saline or H_2O_2. Peroxide induced an increase.

19. Ethane production from isolated perfused rat lungs after intratracheal instillation of either saline or H_2O_2. Peroxide increased production.

20. Wet to dry lung weight ratios in isolated perfused rat lungs exposed to intratracheal instillation of either H_2O_2 or saline. Peroxide induced an increase.

21. Changes in dynamic compliance over time in isolated perfused rat lungs exposed to the intratracheal instillation of H_2O_2 or saline. Peroxide tended to show reduced compliance.

22. Mesenteric circulation of control GP13 viewed on newly constructed stage. A shows the standard view with two capillaries on the right draining into a venule on the left. B shows the fluorescence view of the same field demonstrating no leak of 150kD FITC dextran.

23. A and B are different intensity light exposures of hepatic sinusoids of the control GP13 on which two Kupffer cells are scarcely visible at 3 and 6 o'clock. C shows the fluorescence image at the same field after phagocytosis of 0.8μ latex particles. The Kinetics and amplitude of the phagocytic process are thus easily tracked by such on line tracking procedures.

24. Control GP13 mesenteric venules. These twenty micro diameter venules are where capillary leakage is known to occur following treatment with such agents as histamine or bradykinin. A shows the standard image, and B shows complete retention of 150kD FITC dextran by these normal venules.

25. In contrast to normal maintenance of 150kD FITC dextran shown in Figures 22B and 24B, these fluorescent views of mesenteric venules demonstrate the effects of topical TNF at 45 to 47 minutes. A shows bright extravascular areas of blot hemorrhages. B shows diffuse leak of the dextran. These changes might be expected to be seen with Pichinde Virus infection, and can be tracked on line.

Figure 1

CONTROL GP13 HISTOGRAM FOR σ
MEAN σ = .728 ± .018 SEM
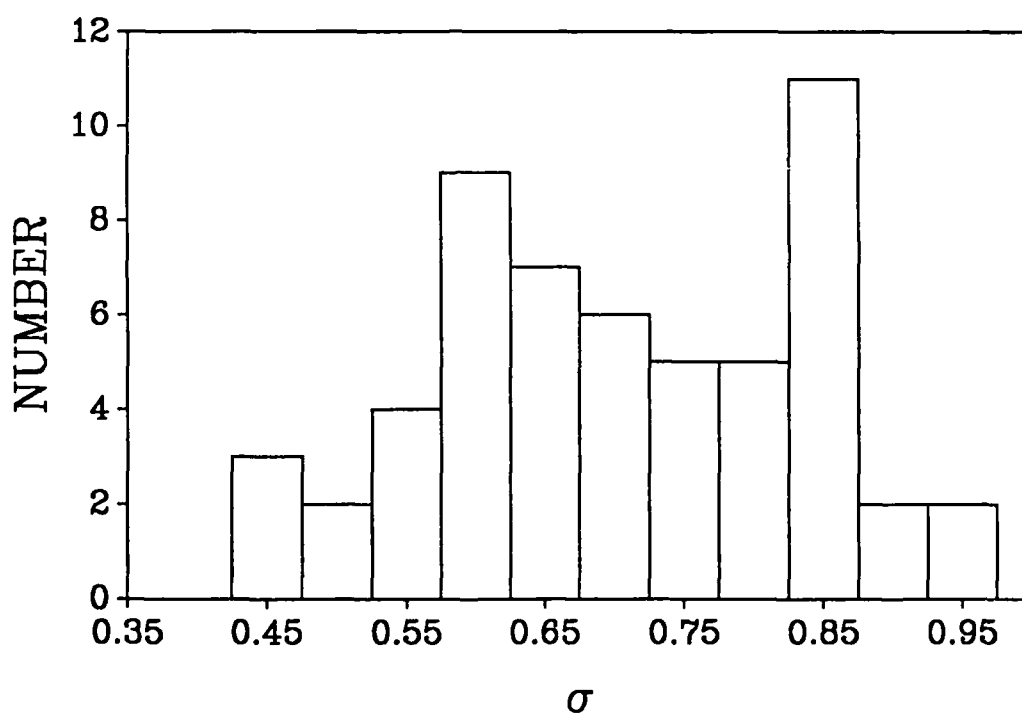
Figure 2

CONTROL GP13 HISTOGRAM FOR PS
MEAN PS = 3.21 ± .29 SEM
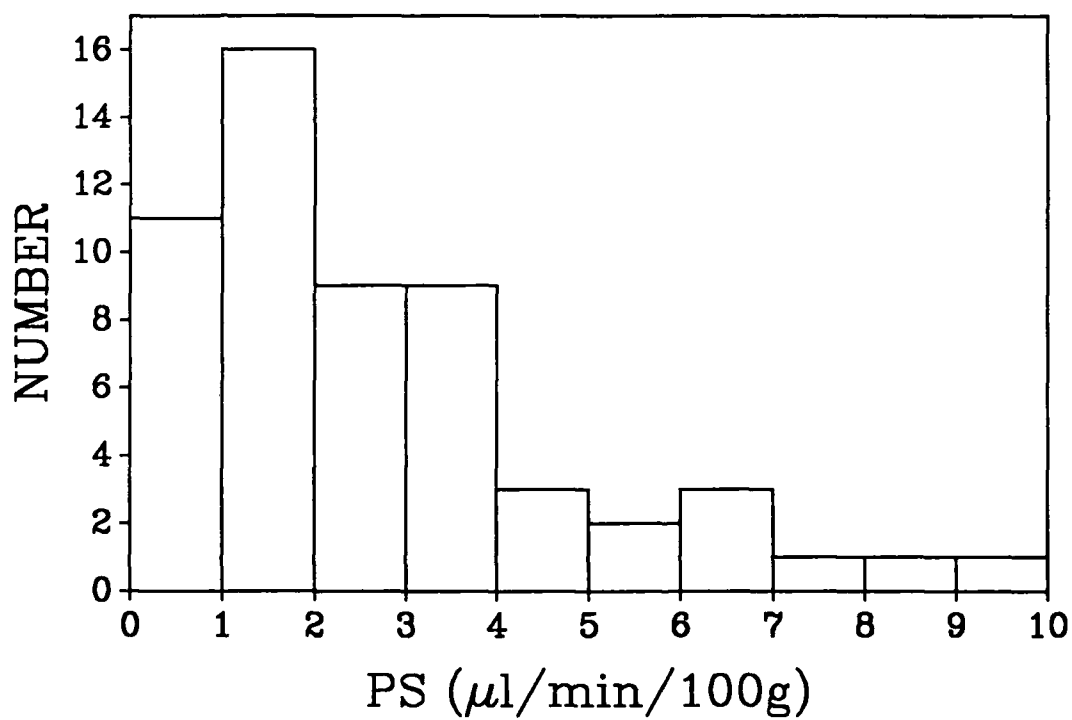
Figure 3
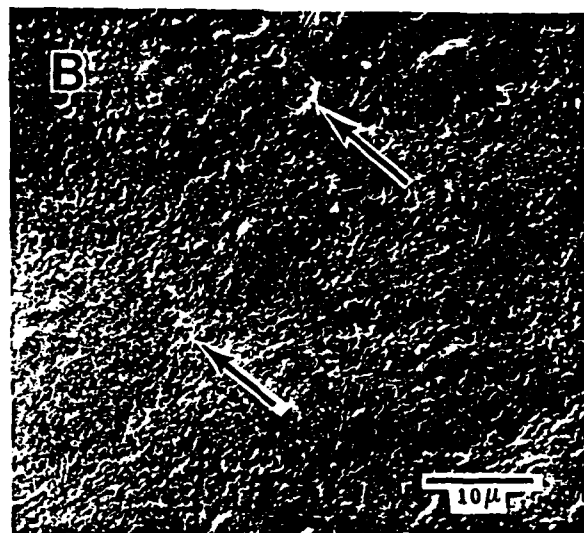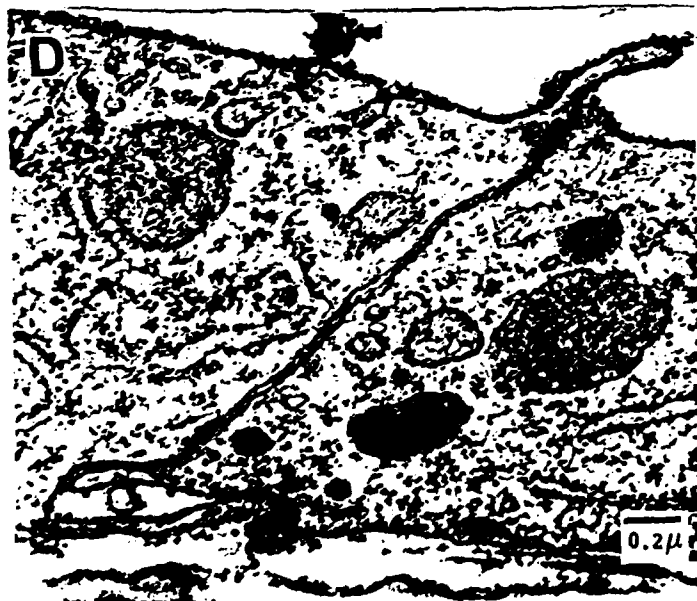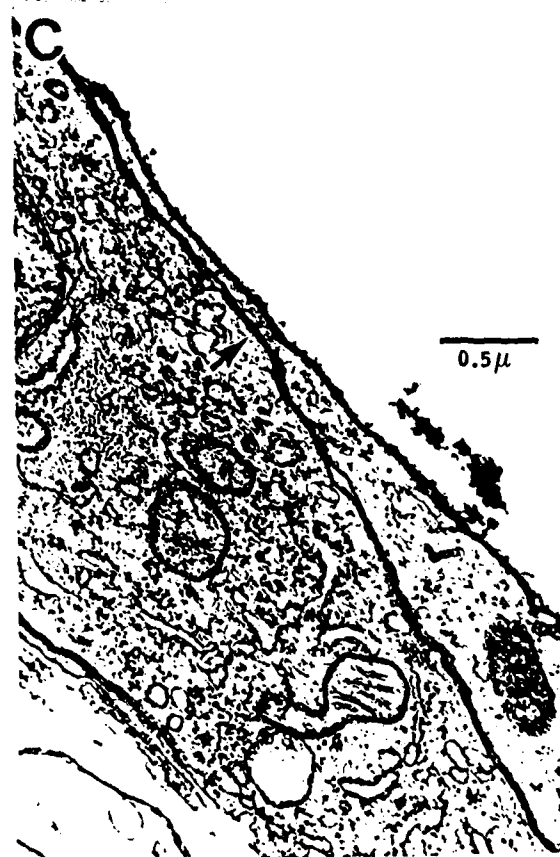
Figure 4
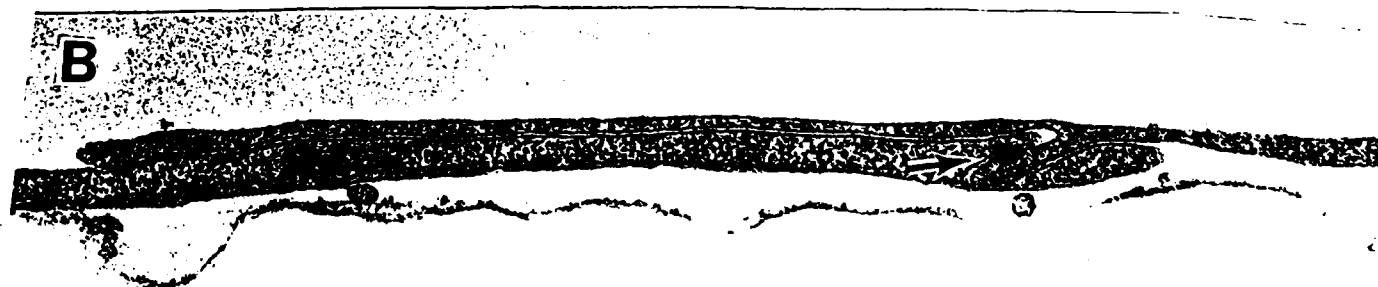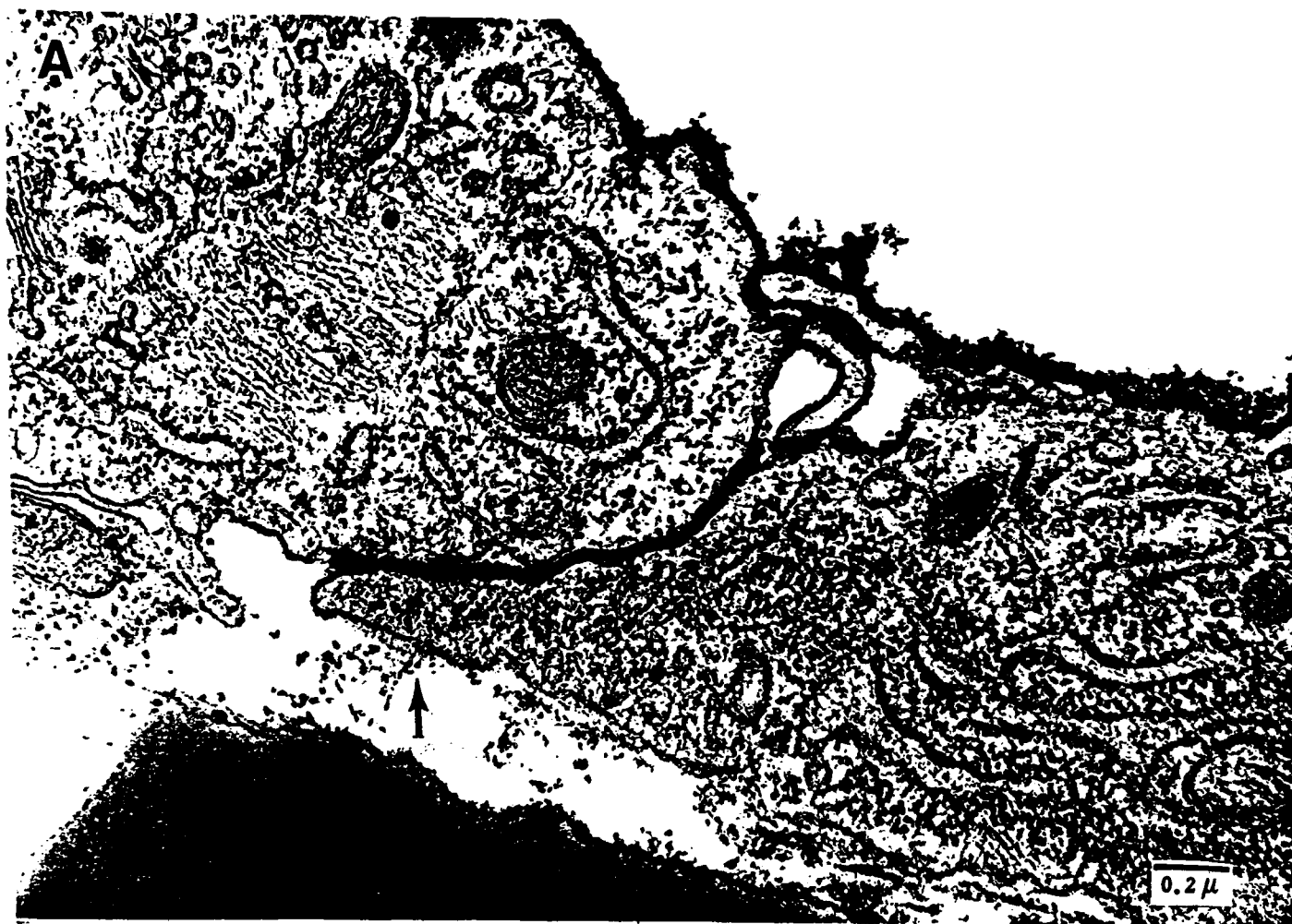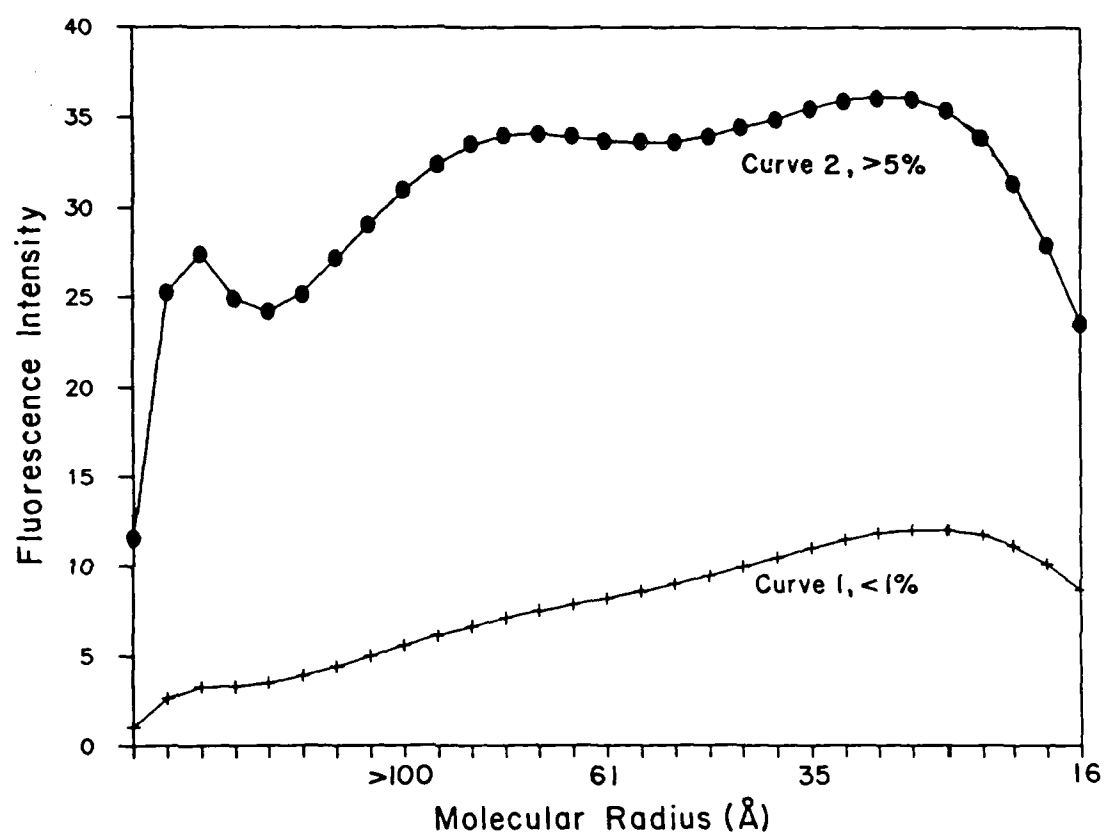
Figure 5

Figure 6
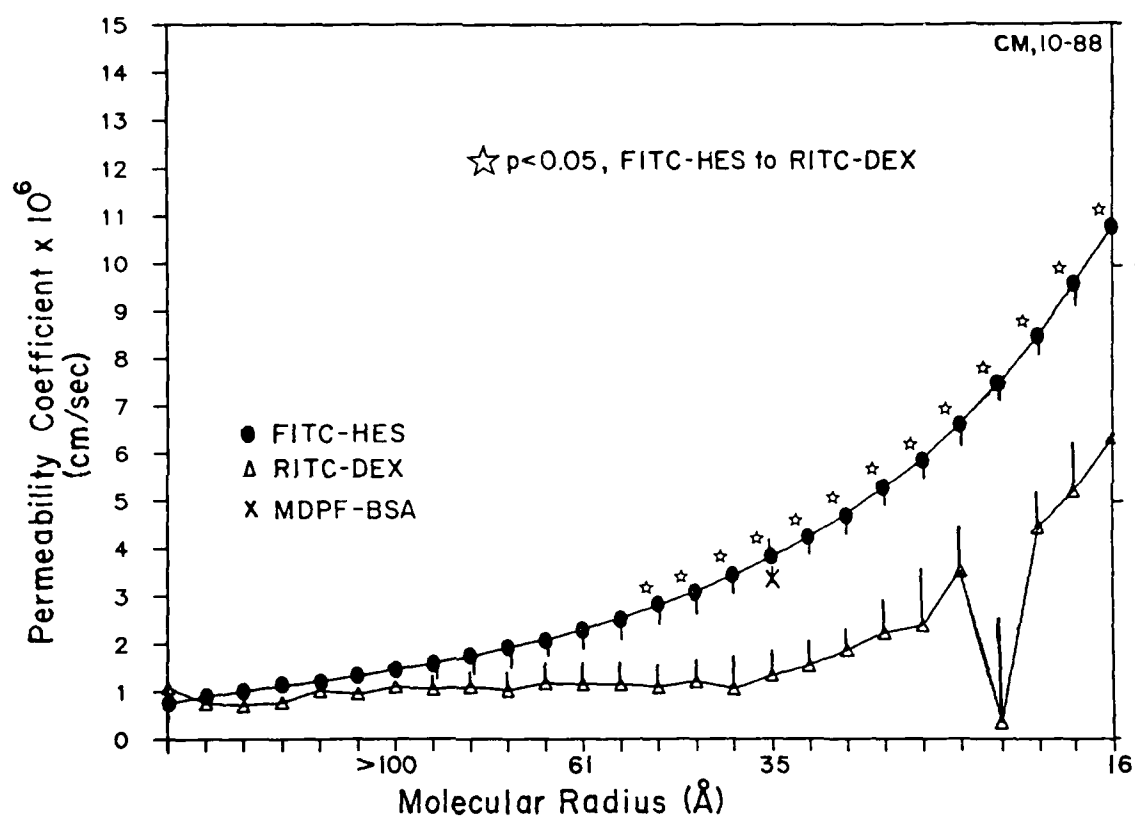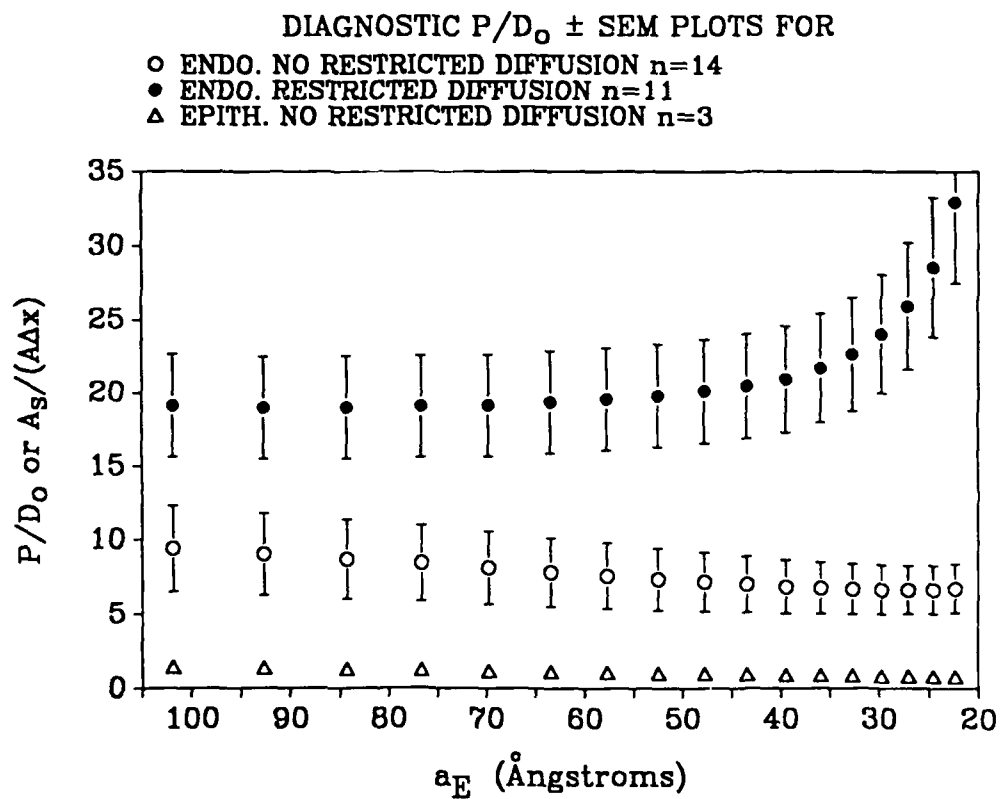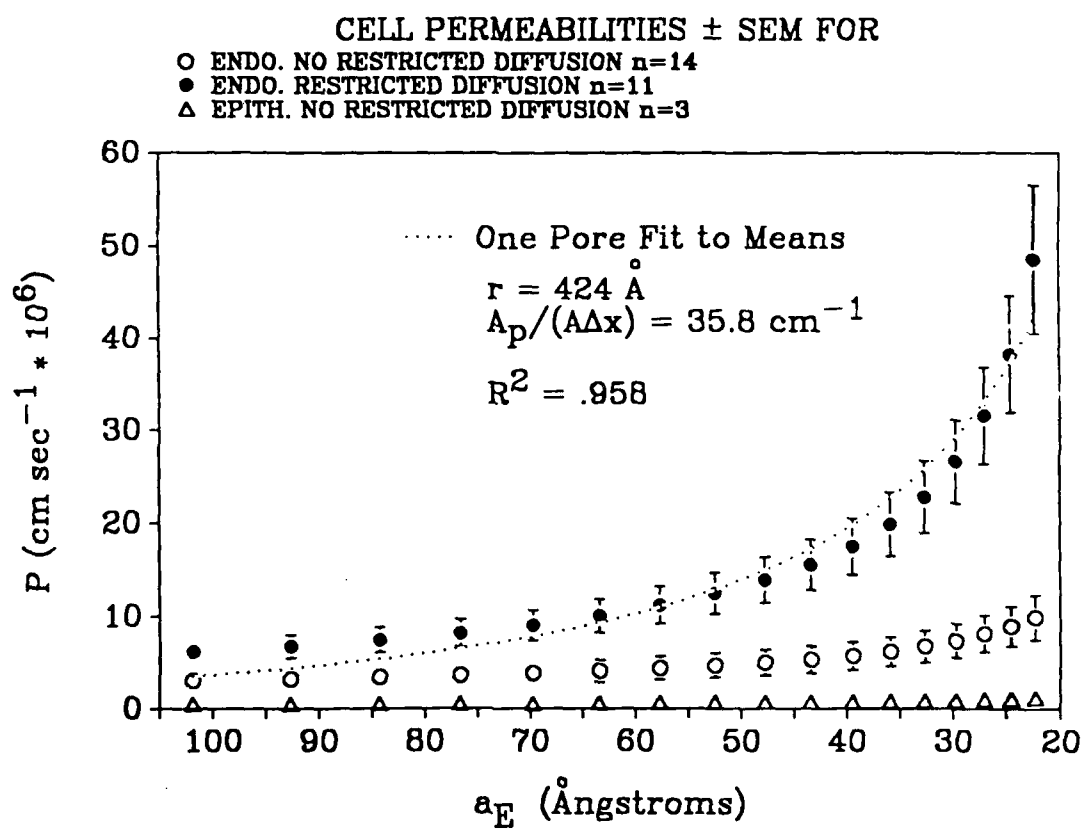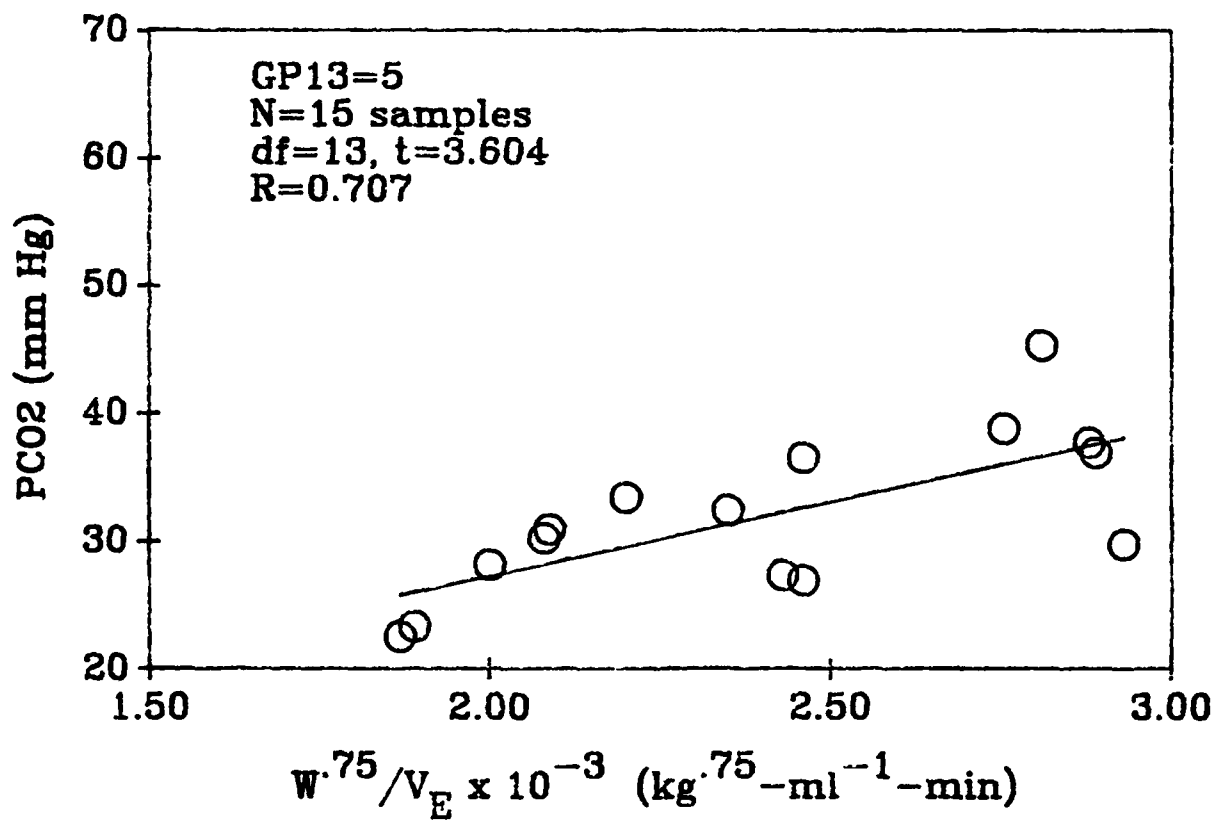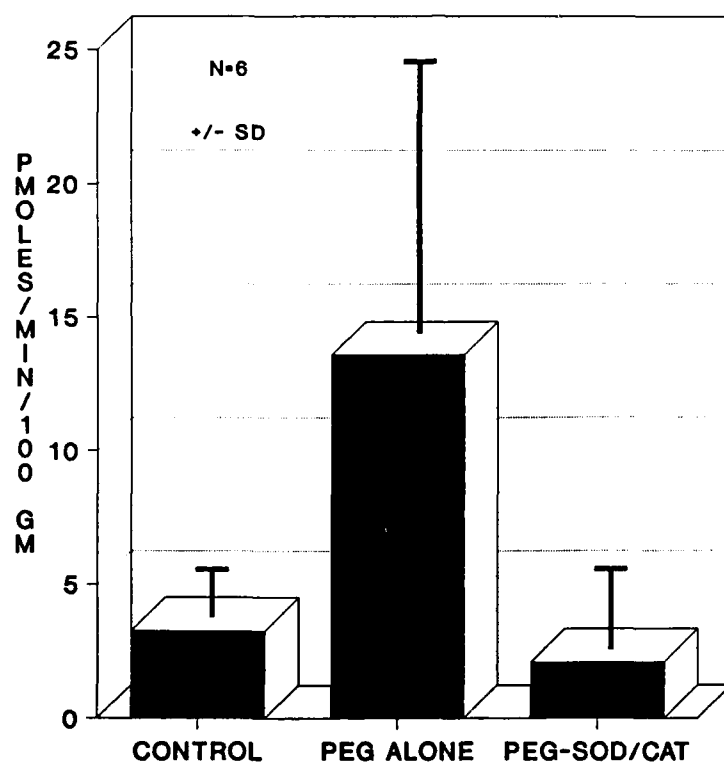
Figure 7
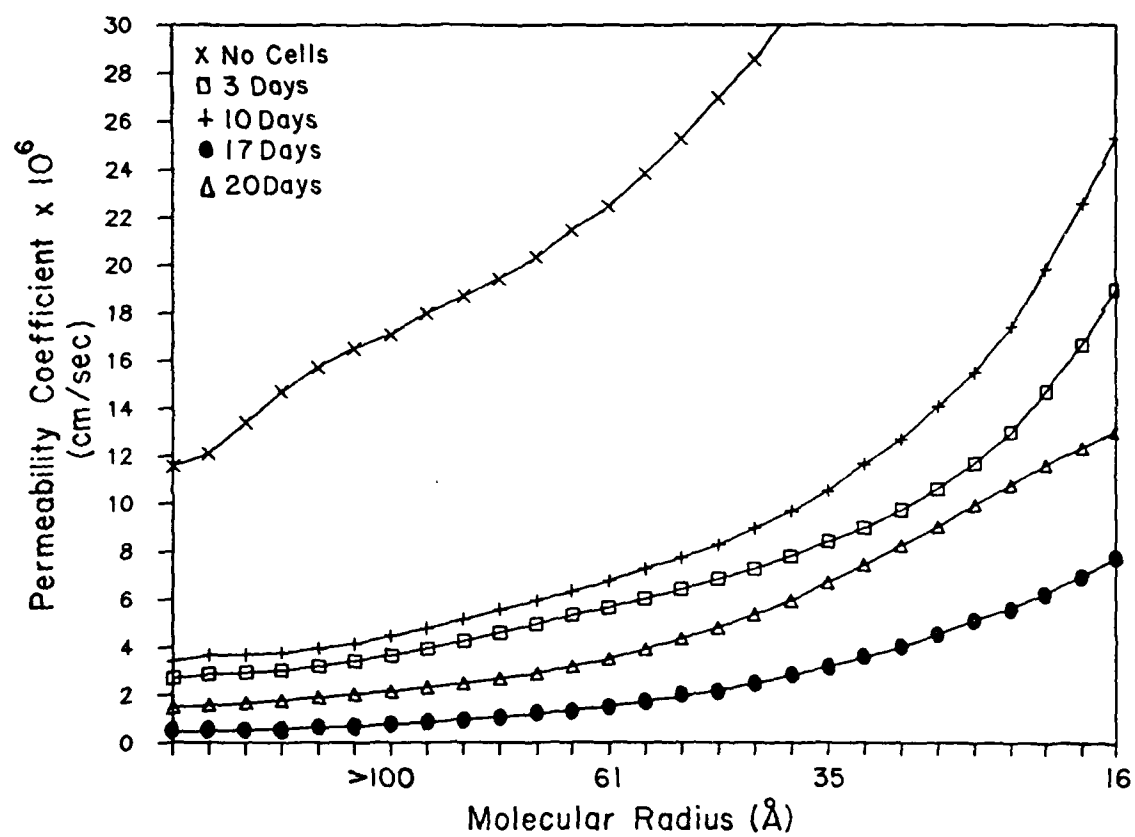
Figure 8

Figure 9

Figure 10

DIAGNOSTIC P/D_O ± SEM PLOTS FOR

○ ENDO. NO RESTRICTED DIFFUSION n=14
● ENDO. RESTRICTED DIFFUSION n=11
△ EPITH. NO RESTRICTED DIFFUSION n=3

Figure 11

CELL PERMEABILITIES ± SEM FOR
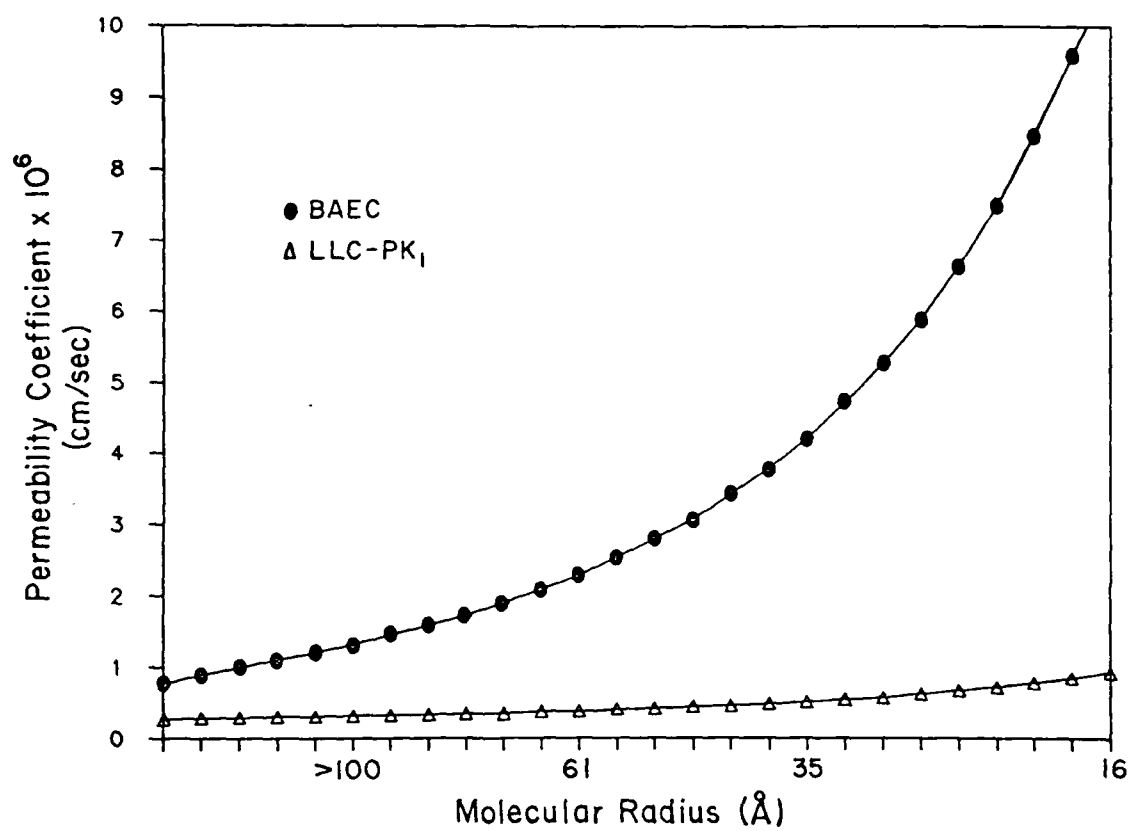
Figure 12

Figure 13

Figure 14

Figure 15

MEAN ETHANE PRODUCTION RATE

HYDROCARBON FREE AIR

Figure 16

PERCENT CHANGE IN ETHANE PRODUCTION

DUE TO O2 IN CONTROL AND EXSANGUINATED RATS
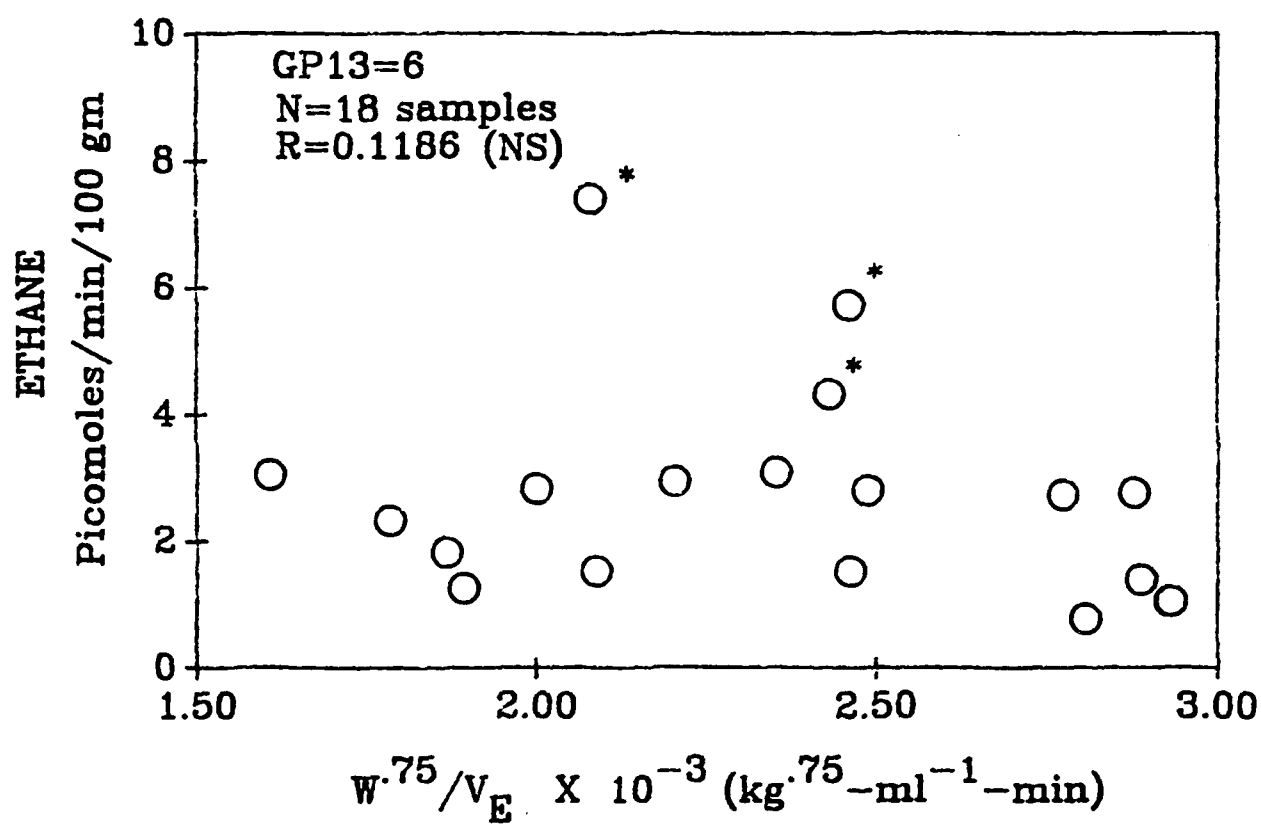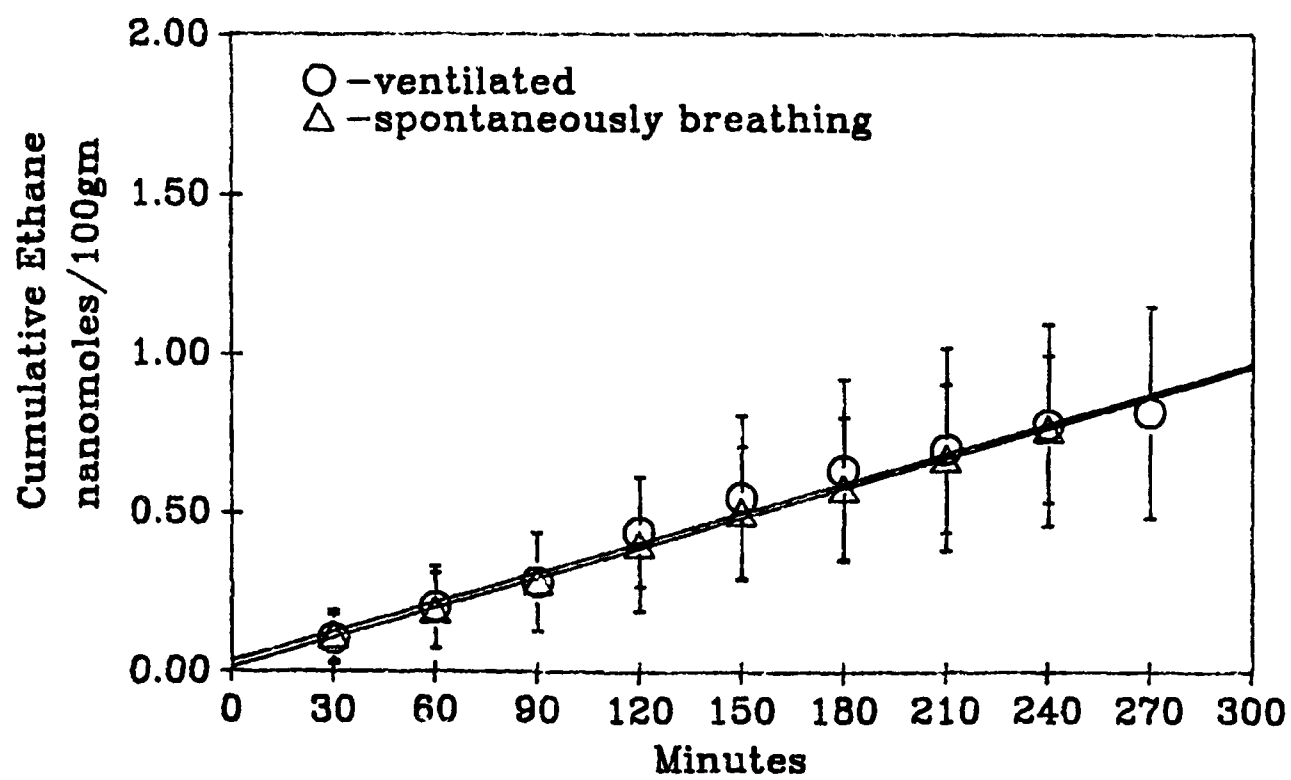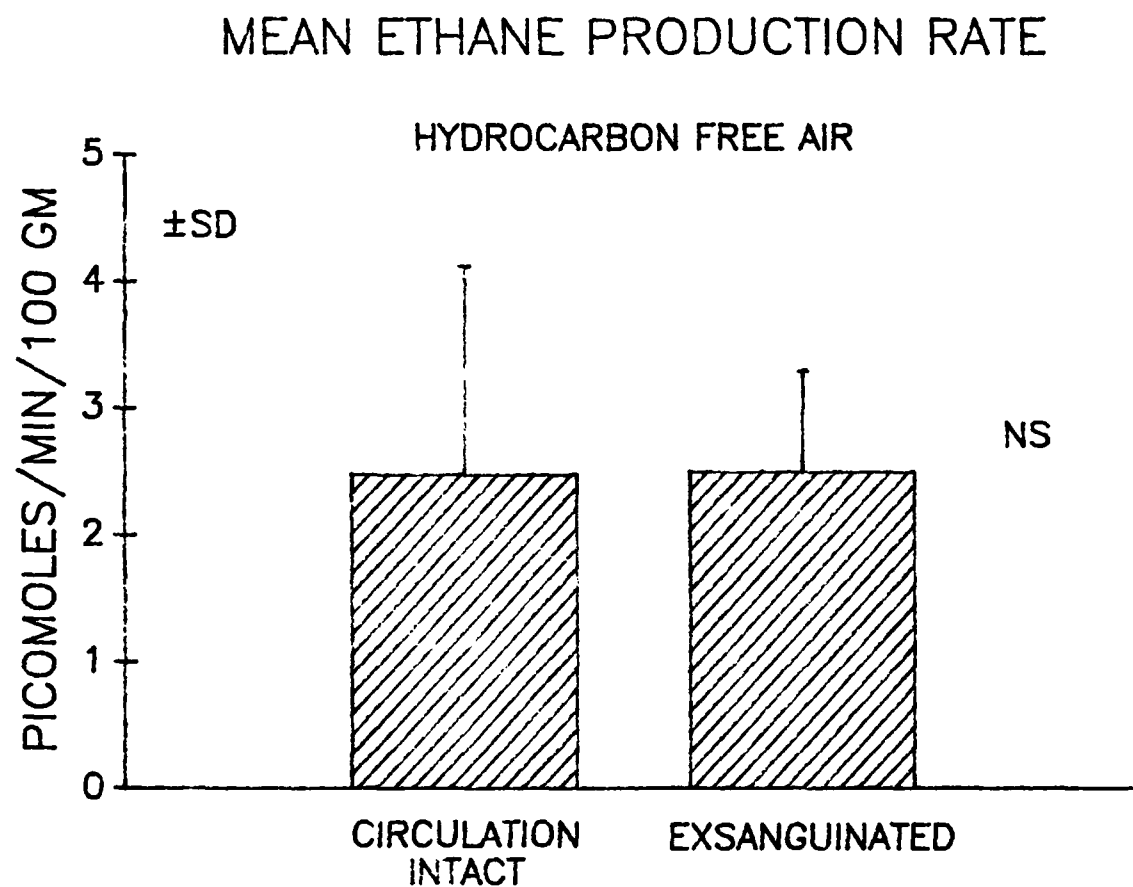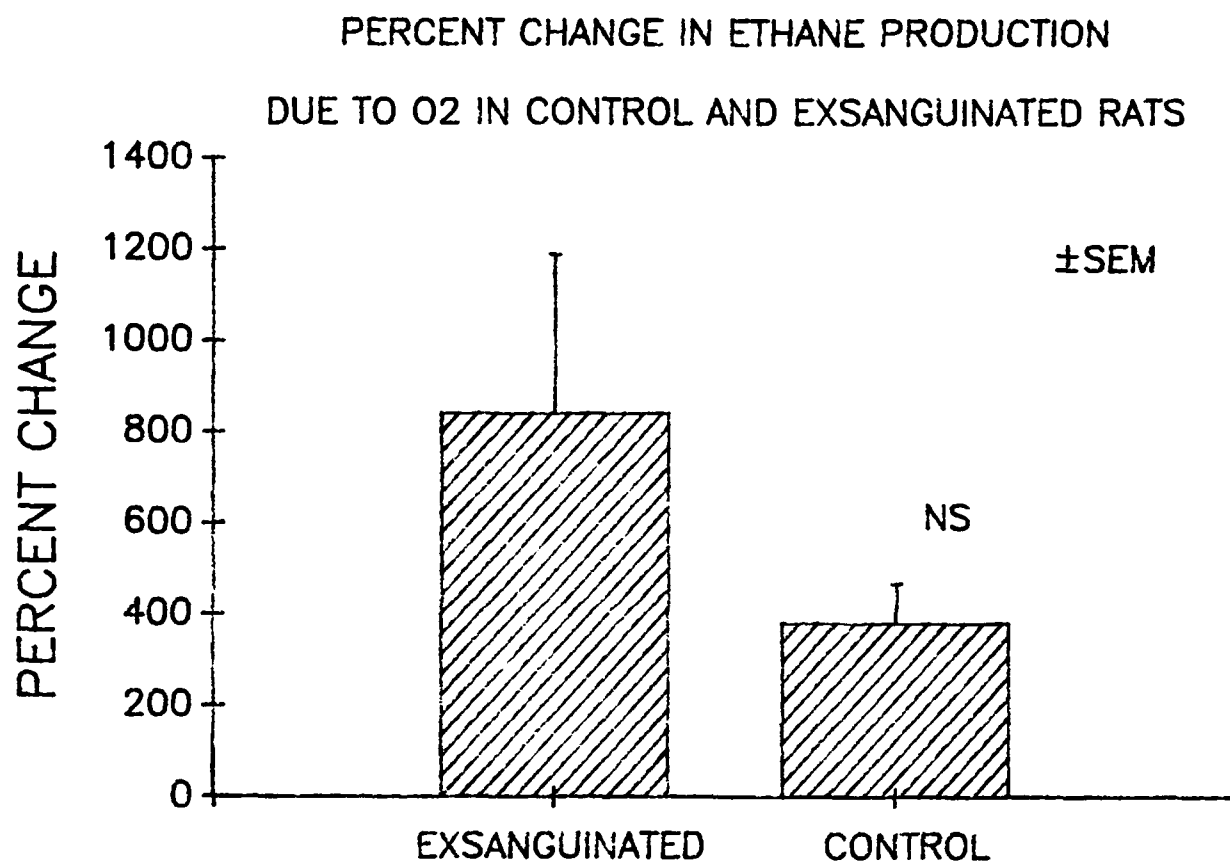
Figure 17

ETHANE PRODUCTION
CHANGE (HFA TO O2)

Figure 18

CONJUGATED DIENES
isolated perfused rat lung

Figure 19

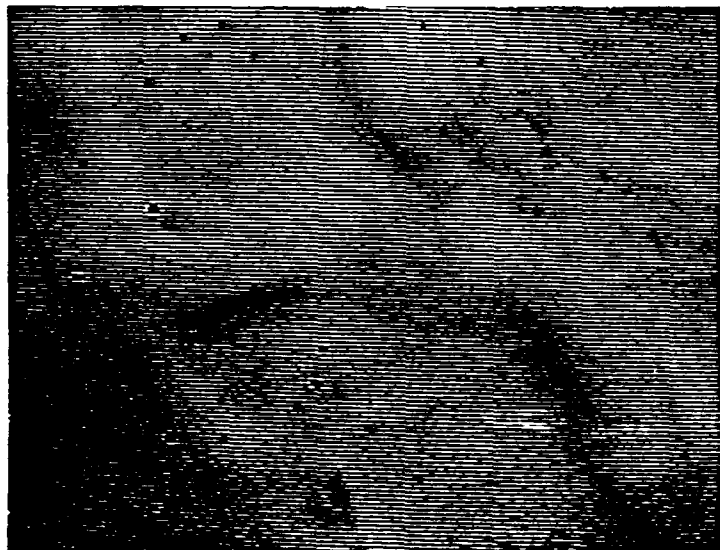ETHANE
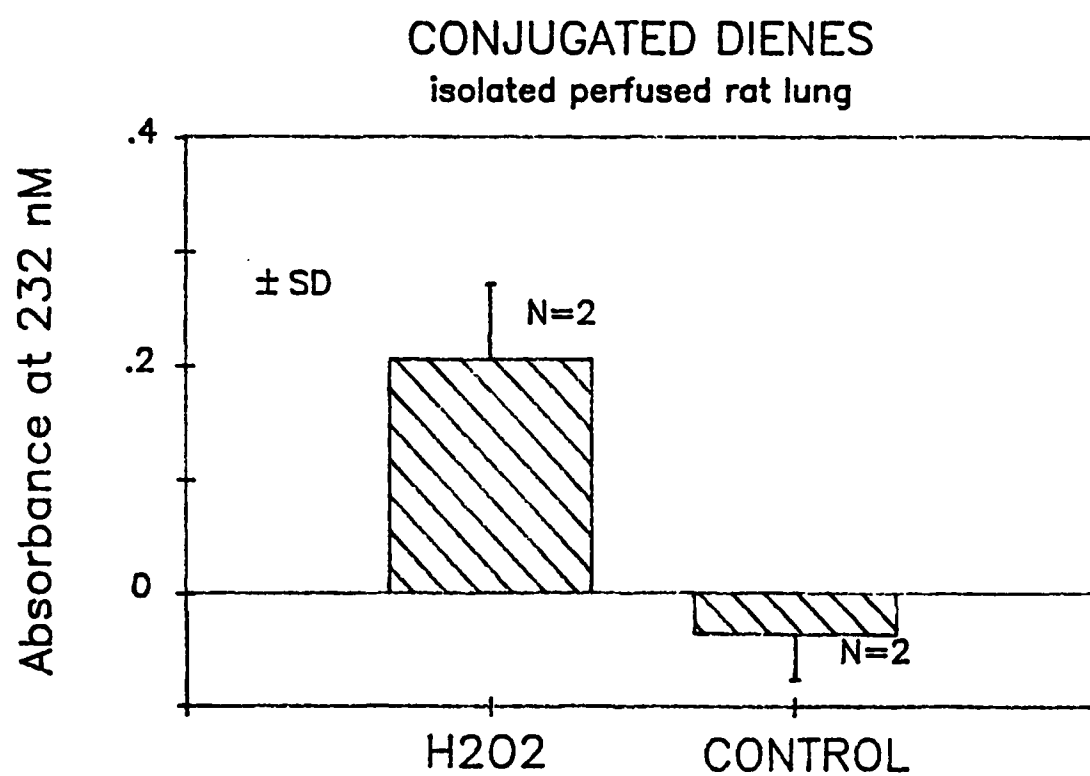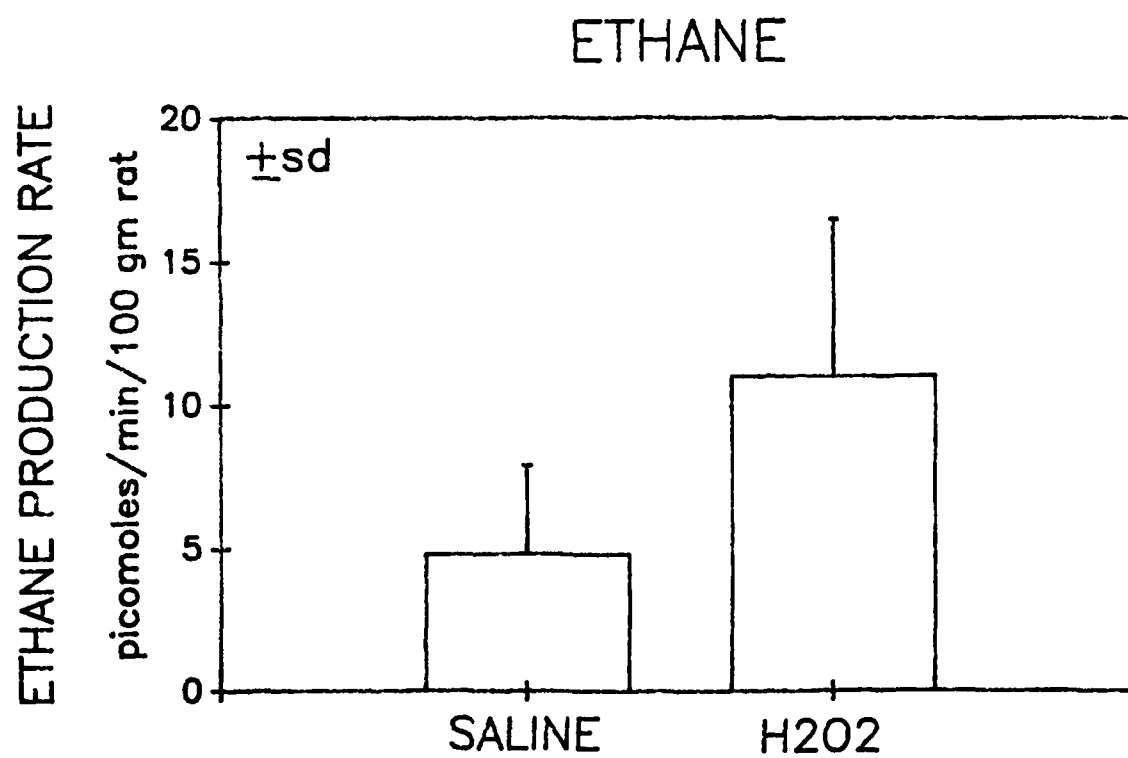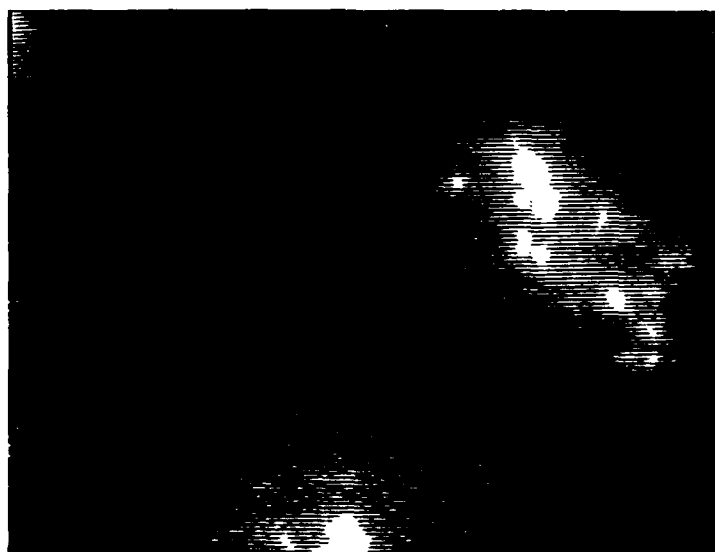
Figure 20

Figure 21

DYNAMIC COMPLIANCE
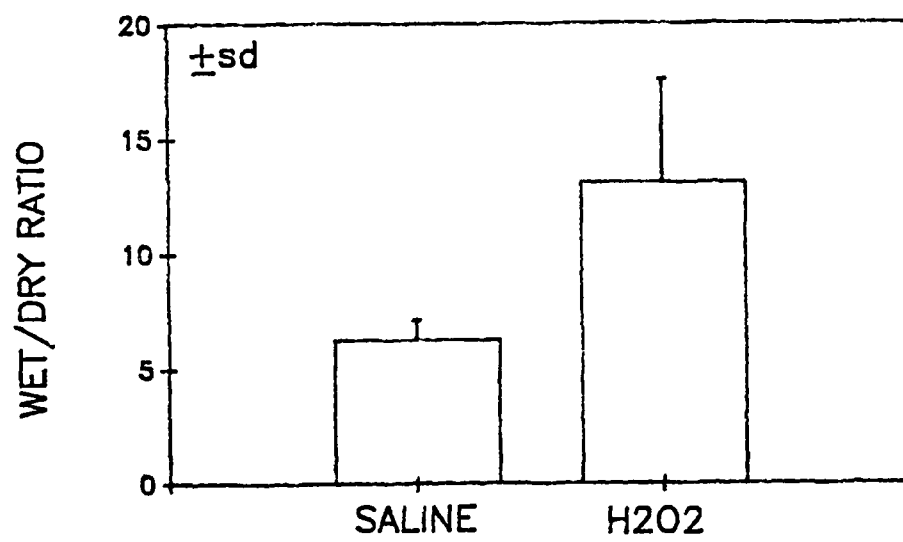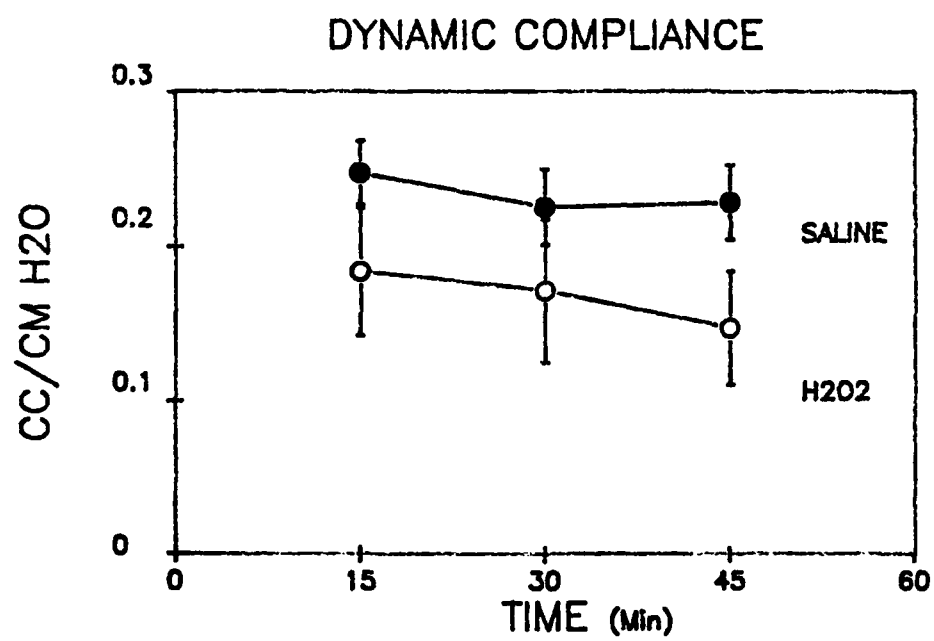
Figure 22

A
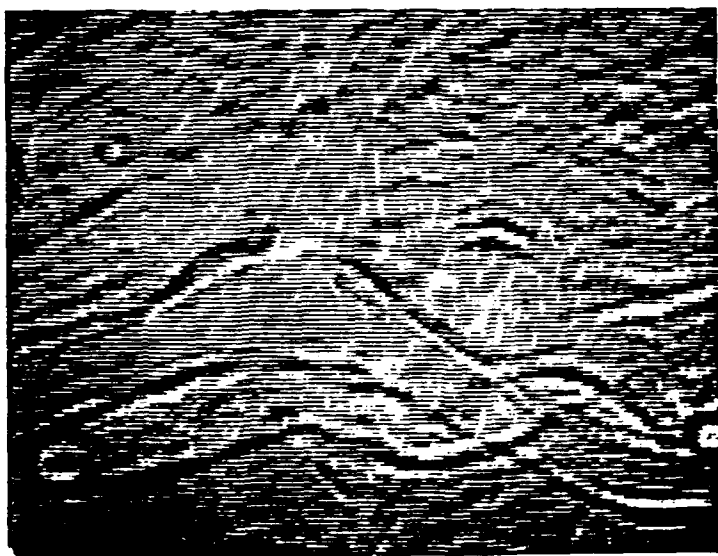
B
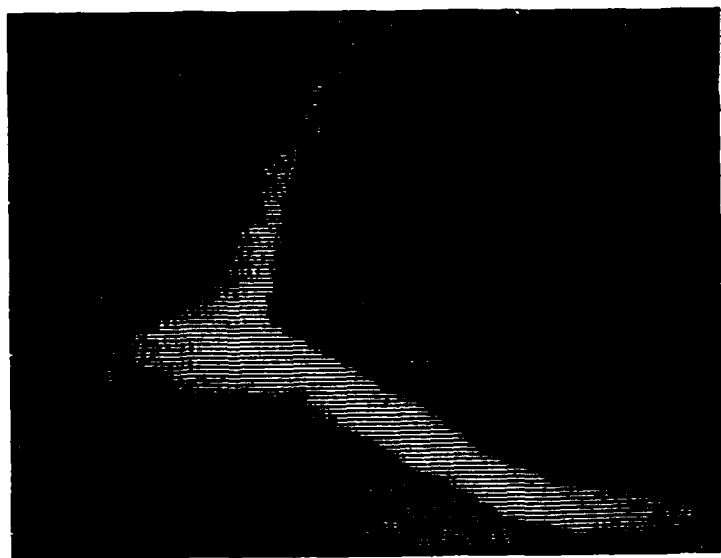
Figure 23

A

B

C

Figure 24

A

B

Figure 25

A
B